NTNU
Norwegian University of
Science and Technology

Control of Eddy-Current Brakes

Snorre Hukkelås

Master of Science in Industrial Cybernetics
Submission date: June 2018
Supervisor: Morten Dinhof Pedersen, ITK

Norwegian University of Science and Technology
Department of Engineering Cybernetics

NTNU – Trondheim
Norwegian University of
Science and Technology

Faculty of Information Technology and Electrical Engineering
Department of Engineering Cybernetics

MSC THESIS DESCRIPTION SHEET

Name:	Snorre Hukkelås
Department:	Engineering Cybernetics
Thesis title (Norwegian):	Styring av virvelstrømbremser
Thesis title (English):	Control of Eddy-Current Brakes

Thesis description: The purpose of this thesis is to design, implement and test an experimental testbed for electronically controlled eddy current brakes (ECBs).

Eddy current brakes enable contact-free torque generation with as little as one moving part. Their indefinite service life and simple construction makes the technology attractive for a wide array of applications, such as railroad brakes, exercise equipment and power tools.

The rig that is to be designed will enable future research on real-time closed-loop precision control of eddy-current braking forces. To achieve this, instrumentation should be implemented so that theoretical models may be validated. Furthermore, a suitable computer interface must be designed so that new control methodologies can be tested experimentally.

The following elements will form part of the thesis:

1. *Design, implementation and testing of an experimental eddy current braking testbed.* A detailed discussion of the experimental setup will be provided, including; electrical engineering, mechanical engineering, instrumentation as well as the real-time control environment.
2. *A survey of models capable of representing the eddy current braking torque.* Relevant models will be simulated and compared to experimental data from the eddy current braking testbed.
3. *Demonstration of real-time torque control.* The ultimate goal of the thesis is to facilitate future research on ECB devices. In order to show that this aim has been achieved, real-time torque control should be demonstrated experimentally.
4. Salient experimental and theoretical findings are to be presented in the final report.

Start date: 08.01.2018
Due date: 18.06.2018

Thesis performed at:	Department of Engineering Cybernetics, NTNU
Supervisor:	Associate Professor Morten D. Pedersen

Preface

This thesis is submitted in fulfilment of the requirements for the degree of Master of Science at the Department of Engineering Cybernetics of NTNU, specifically the two year master program on Industrial Cybernetics. The program gives basic knowledge within the key topics of cybernetics, enabling the student to specialize in a field determined by his or her bachelor's degree, which in the author's case is Mechanical Engineering.

The practical implementation which was done in this thesis was a collaboration between the author and the workshop at the Department of Engineering Cybernetics at NTNU, the author contributed with:

- Conceptual sketches and computer aided design (CAD) of the eddy current braking testbed.
- Dimensioning of the rotating conductive disc and the electromagnet cores.
- Winding of the electromagnet cores.
- Indicative information about motor requirements.
- Computer aided design, 3D printing and assembly of a permanent magnet mount.
- Computer aided design, 3D printing and assembly of a chain tightening mechanism.
- Hardware selection and ordering, including: transistors, diodes, resistors, microcontroller and capacitors.
- Selection and installation of data acquisition(DAQ) software.
- Indicative information about power supply requirements.
- Finalizing the lab setup, including: Wire hookup and wire crimping, soldering, mounting the force sensor and all breadboard prototyping.
- Taking measurements with multimeter, oscilloscope, gaussmeter and LCR meter.
- Troubleshooting.

The workshop contributed with:

- Finalizing the design according for manufacturing feasibility.
- Design of motor bracket.
- Final selection and ordering of DC motor.
- Design of electromagnet fastening method.
- Machining and final assembly, including: Disc, shaft, side plates, bottom plate, motor with bracket, bicycle cassette, chain, force sensing bracket and magnetic cores.
- Supplying LCR meter, gaussmeter and power supplies.
- Lab space.

Solidworks, Matlab and Simulink were used for computer aided design, calculations and as the control environment, respectively. The lab at the Department of Engineering Cybernetics at NTNU was used during the implementation and experimentation process.

The thesis advisor assisted with discussion and proof reading of the final report.

Summary

Magnetic braking utilizing eddy currents is used in a wide range of applications. Eddy current braking is done by moving a magnet, either electronically controlled or permanently magnetized, relatively to an electrically conductive material. The existing literature is somewhat intricate and theoretical, and there is a need for bridging the gap between theory and practice. This thesis aims to facilitate practical research by implementing an eddy current braking testbed (ECBT), which enables torque measurement for model validation and also real-time torque control.

The ECBT was made out of a large conductive disc spinning in the airgap of two electromagnets, mounted on a shaft that was fastened to a wooden base. A permanent magnet was also tested for comparison. The disc was driven by a DC motor and a chain drive, controlled by a PI-controller. Braking force measurements were done with the help of a force sensing mechanism that outputted an analog signal proportional to the braking force. The system was monitored and controlled with a microcontroller of the type Arduino Mega2560, running code produced in Simulink with the help of the Arduino Support Package made by MathWorks. Data was stored after each test and post-processed in Matlab.

The final ECBT is to be considered as a first prototype of such a system, with some potential improvement areas. Deviations from theory were seen, something that is thought to be caused by a great deal of magnetic fringing in the air gap and possibly uncertainties in disc conductivity. Several interesting magnetic phenomena were encountered that must be considered when designing and controlling electromagnetic brakes. Finally, a torque control demonstration using a sliding mode controller showed the ECBT's ability to perform real-time torque control.

The findings presented in this thesis highlight several important factors to consider when designing eddy current braking systems. The final system was made functional and it is the hope that this thesis may be an aid to future researchers doing work on electromagnetic braking.

Sammendrag

Magnetisk bremsekraft ved å utnytte virvelstrømmer er brukt i et vidt spekter av applikasjoner. Denne typen bremsing gjøres ved å bevege en magnet, enten elektronisk kontrollert eller ved hjelp av en permanentmagnet, relativt til et elektrisk ledende materiale. Den eksisterende literaturen kan oppfattes som kompleks og teoretisk, og det er et klart behov for å sy sammen teori og praksis. Denne avhandlingen søker å legge til rette for forskning ved å implementere et testoppsett for eksperimentering på virvelstrømsbremser, som muliggjør måling samt sanntidskontroll av bremsekraft.

Testoppsettet ble laget av en disk som roterte i luftgapet på to elektromagneter, rundt en aksling montert på en treplate. En permanentmagnet ble også testet for sammenligning. Disken ble drevet av en DC motor via et kjede, og kontrollert av en PI-kontroller. Bremsekraft ble målt ved hjelp av en sensormekanisme som ga et analogt signal proporsjonalt med bremsekraften. Systemet ble monitorert og kontrollert av en mikrokontroller av typen Arduino Mega2560, som kjørte kode generert av Simulink ved hjelp av Arduino Support Pakken lagd av MathWorks. Data ble lagret etter hver test og deretter prosessert i Matlab, for blant annet sammenligning med teoretiske verdier.

Det resulterende testoppsettet sees på som den første prototypen av et slikt system, med noen forbedringspotensialer. Det ble sett avvik fra teoretiske verdier, og grunnen til dette ble antatt å være en stor grad av ujevnhet i den magnetiske flukstettheten i luftgapet mellom polene og muligens usikkerheter når det kom til diskmaterialets konduktivitet. Flere interessante magnetiske fenomener ble vist, som bør tas hensyn til ved design og kontroll av elektromagnetiske bremser. Til slutt ble det demonstrert sanntidskontroll av bremsekraft ved hjelp av en sliding mode kontroller.

Resultatene presentert i denne avhandlingen fremhever flere viktige faktorer man må ta hensyn til ved design av virvelstrømsbremser. Systemet ble gjort funksjonelt, og vil forhåpentligvis være en hjelp til fremtidige forskere som ønsker å arbeide med elektromagnetisk bremsing.

Acknowledgements

I would like to thank my supervisor, Morten D. Pedersen for being a supportive motivator, guiding me along the way and for helping me with the last touches on the final report. I also want to thank the workshop at the Department of Engineering Cybernetics at NTNU for providing lab space, for helping me to obtain suitable parts and for their great job on the ECBT.

A special thanks goes out to my girlfriend for her patience, support and stress relieving presence, especially during the run-up of my studies. Thank you to my family and friends for their patience and unlimited support through these years of education. Thank you to my classmates for inspiring conversations and helpful advice, and for contributing to a great study environment.

Contents

List of Figures

List of Tables

Chapter 1

Introduction

1.1 Readers Guide

The structure of the thesis can be outlined in the following way:

- Chapter 1 aims to motivate the reader by presenting background information about eddy current braking and its applications.
- Chapter 2 provides the reader with some necessary theoretical concepts and a survey of the existing literature on the subject of electromagnetic braking.
- Chapter 3 goes through the design and implementation process of the eddy current braking testbed (ECBT), while discussing issues continuously. Finally, the resulting prototype is presented.
- Chapter 4 gives basic insight into control theory and how it can be used to control ECBs, along with a presentation of existing work. This chapter forms a basis for torque control demonstration.
- Chapter 5 discusses the experimentation process along with a presentation and discussion of the results.
- Chapter 6 concludes the thesis and gives recommendations for further work on the ECBT.

The reader is expected to have a basic understanding of physics and engineering topics such as electrical, mechanical and control engineering.

1.2 The History of Contactless Braking

Braking technology is important to a vast amount of mechanical systems. Halting or doing speed control on rotating components in a safe, controllable and sustainable manner could be critical for optimizing the feasibility of a system and to extend its working lifespan. There are many ways of designing a braking system, and up until recent years the most common approach has been to use electric, hydraulic or mechanical systems to press specially designed braking pads up against the moving component. An example of this can be seen on bicycles, where brake pads are used to clamp against a metal disk that is attached to the wheel. This clamping action results in frictional torque that opposes the rotational motion and converts the mechanical energy into heat. There exist one special phenomena of electromagnetism that is being used in many modern braking applications, and this phenomena is known as eddy currents. The use of eddy current brakes (ECBs) has clear advantages over traditional systems, as they are practically friction free, require few moving parts and therefore little too no maintenance. The reduction of moving parts increases lifespan and eases implementation, while also maximizing response time.

Eddy currents are exploited in a wide range of commonly known applications. Their reliability in all kinds of weather along with low maintenance requirements makes magnetic braking systems a safe choice compared to pure mechanical or hydraulic systems. The auto belay, which is a device that assists climbers in a descent by lowering him or her in a safe and controllable manner, often use eddy current braking. Emergency shut off is another application that many modern industrial power tools make use of. Magnetic braking provides a smooth way of adjusting resistance, and is therefore often used in exercise devices. As anyone who has tried an indoor rowing machine would know, the resistance increases as you pull harder to mimic the feeling of rowing in water, and this is often obtained by using eddy current brakes in the apparatus.

Smythe [1, 1942] was the first to examine the theoretical relationship between torque and rotational velocity in an eddy current brake, by using Maxwell's formulas to derive an equation for a large disk, of a finite radius, rotating between a pair of circular poles of an electromagnet. Following Smythe, several others worked on developing analytical models of eddy current brakes. Schieber [2] layed out a model that was in agreement with Smythe's work, in addition to describing an experimental setup in which he compared the results. He also provided a numerical solution to the problem, and found good agreement between theory and experiments. Wiederick et al. [3] used Ohm's law and Lorentz's Force law to obtain the drag forces working on a pole projection area moving linearly relative to a conductive sheet of infinite length, neglecting special effects that occur in the air gap between the pole and conductor. Wiederick's simplistic model was later revised and improved by Heald [4], by introducing a compensatory factor accounting for the behavior at the edge of the pole. Using existing theory (e.g.

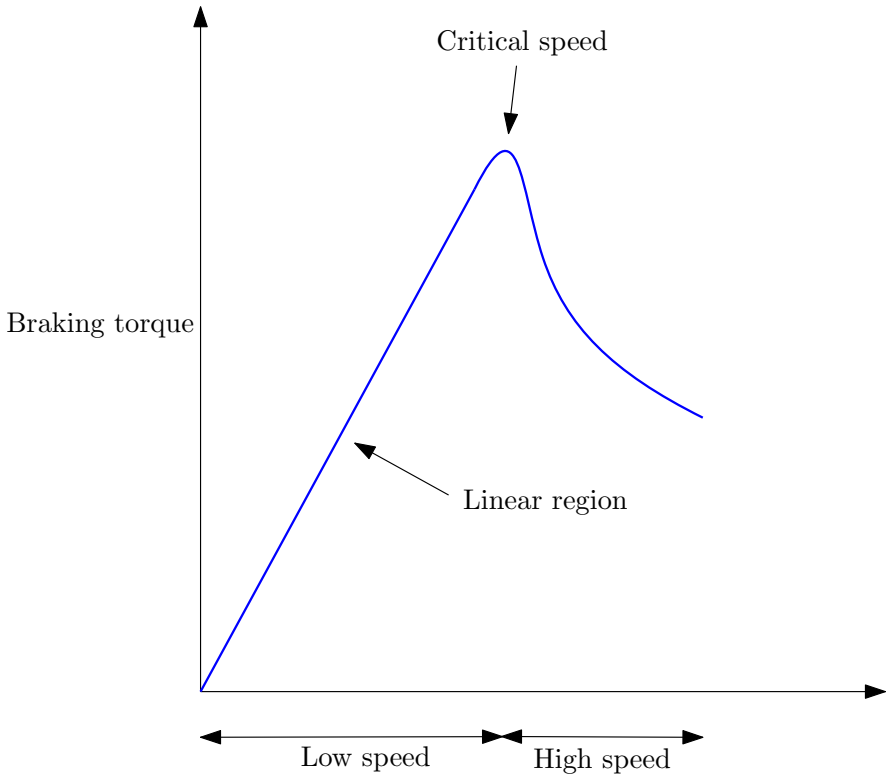

Figure 1.1: The different speed regions of magnetic braking.

[5] and [6]), Simeu and Georges [7] applied a non linear control scheme to achieve speed control by using an eddy current brake, proving the feasibility of such a system. Using Wouterse [5], Wiederick et al. [3] and Heald [4], Barnes et al. [8] created a computer model of braking systems for use in exercise devices. Solving eddy current problems by numerical solutions, i.e. FEM[1], has also been a topic investigated by scientists like Peterson [9], Burais et al. [10], and Conraths [11]. The use of eddy current braking has mostly been restricted to higher rotational speeds due to the fact that the torque is proportional to the speed below a certain threshold and lower speed therefore means lower braking torque, see Figure 1.1. According to Karakoc et al. [12], Lee et al. [13] was the first to apply an alternating field to address this problem. Following up on this idea, Karakoc et al. [12] further explored AC based magnetic field application, by testing different kinds of waveforms and implementing frequency modulation. According to their results an increase of 60% in braking torque was seen when applying a triangular waveform via frequency modulation compared to a regular DC field.

[1]FEM = Finite Element Analysis.

Chapter 2

Theory and Background

2.1 The Eddy Current Phenomena

Knowing some basic properties of electromagnetism is key to understanding the existing literature and the physics behind eddy current braking.

Faraday's law of induction (2.1) is the principle that lies behind electric power generators. It tells us that when the magnetic field density $\mathbf{B}$ is changed through time an electric field $\mathbf{E}$ is created. For example, moving a magnet along a conducting wire will cause the magnetic field to change and the resulting electric field will cause electric currents to flow. These currents give rise to their own magnetic field. *Lenz's law* states that the direction of the induced electric field has a direction such that it opposes the field that created it:

$$\nabla \times \mathbf{E} = -\frac{\partial \mathbf{B}}{\partial t} \tag{2.1}$$

Ampère's law (2.2) can be regarded as the reverse of Faraday's law, stating the characteristics of the magnetic field that is caused by an electric field, e.g. the magnetic field $\mathbf{H}$ created around a current conducting wire:

$$\nabla \times \mathbf{H} = \mathbf{J} + \frac{\partial \mathbf{D}}{\partial t} \tag{2.2}$$

Here $\mathbf{J}$ is the current density in the wire and $\mathbf{D}$ is the electric displacement field.

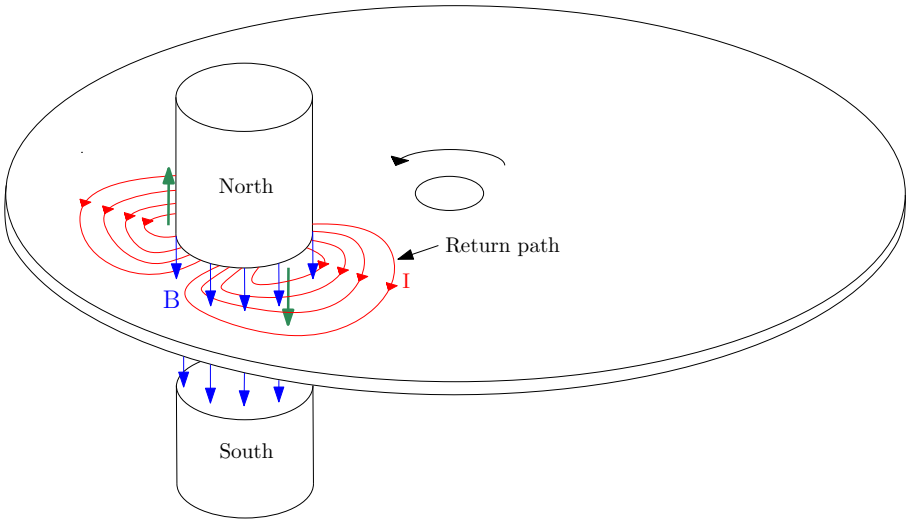

Figure 2.1: A circular disc rotating counterclockwise through the airgap of a stationary magnet. The blue arrows indicate the magnetic field lines (B) flowing from the north to south pole, and the red lines illustrate the eddy currents (I) flowing in the disc as it enters the leading edge (left side) and leaves the trailing edge (right side) of the magnet. The return path of the currents is highlighted because of its relevance to the mathematical modeling of the braking torque discussed in Section 2.3.

Lorentz' force law (2.3) states the relationship between a charged particle moving through a magnetic field and the resulting forces acting upon it. When current is flowing in a conductive material, electrically charged particles move through it and can be used to deduce the direction and magnitude of the resulting forces:

$$\mathbf{F} = q\mathbf{v} \times \mathbf{B} \tag{2.3}$$

Here $\mathbf{F}$ is the force acting on charged particle, $\mathbf{v}$ is the particle speed and $\mathbf{B}$ is the magnetic field density.

Faraday's, Lenz's and Ampere's laws provide a basis for an intuitive understanding of what happens when a conductive material passes through a magnetic field, and thus the working of an eddy current brake. Figure 2.1 illustrates the field lines flow from the north to south pole of a stationary magnet, through a conductive disc rotating counterclockwise. As the disc rotates, the volume under the pole projection area[1] increases in magnetic flux density at the leading edge of the pole(left side) and decreases at the trailing edge(right side). Faraday's law of induction states that any change in a magnetic environment will induce a voltage in the conductive material on which it acts on, and that the current will flow in a plane perpendicular with the field. The exact same thing happens in the disc as it passes through the air gap of the magnet and experiences changes in its magnetic environment. Lenz's law adds that the polarity of the induced voltage and the direction of the resulting current will be such that it opposes the change

[1]The pole projection area defines an area on the disc directly beneath the pole, constricted by the poles' outer rim.

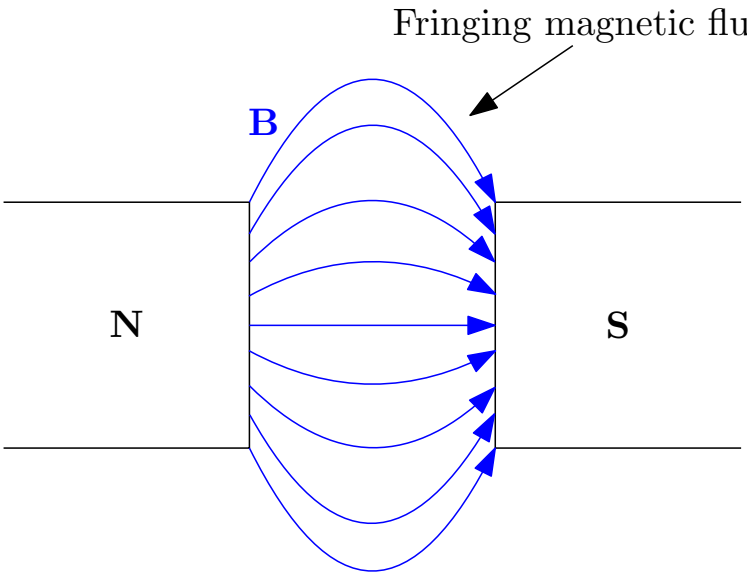

Figure 2.2: The fringing flux in the airgap of a magnet.

at which it is produced. By Amperes law the currents result in swirling patterns that resemble eddy currents in a river, hence the name. This means that the eddy currents at the leading and trailing edge will produce magnetic fields of a direction such that they oppose the motion. Lorentz' force law can be used to explain how these fields produce attractive and repulsive forces between the disc and the magnet at the trailing and leading edge, respectively.

2.2 Properties of Magnetism and Magnetic Materials

2.2.1 Hopkinsons' law

Hopkinsons' law (2.4) is the equivalent of Ohm's law when it comes to magnetic circuits and can be used to approximate the field intensity in the air gap of an electromagnet. It states that,

$$\mathcal{F} = \Phi\mathcal{R} \tag{2.4}$$

Here, $\mathcal{F}$ is the magnetomotive force, $\mathcal{R}$ is the total reluctance of the magnetic circuit and Φ is the magnetic flux that runs through the element, i.e. core. The reluctance is given by,

$$\mathcal{R} = \frac{l}{\mu A} \tag{2.5}$$

Here, μ is the permeability of the material and l is the length of the circuit. This is an idealized tool which applies best to circuits with small air gaps, and the accuracy will be discussed when designing and implementing the electromagnet in Section 3.3.3.

2.2.2 Special Considerations

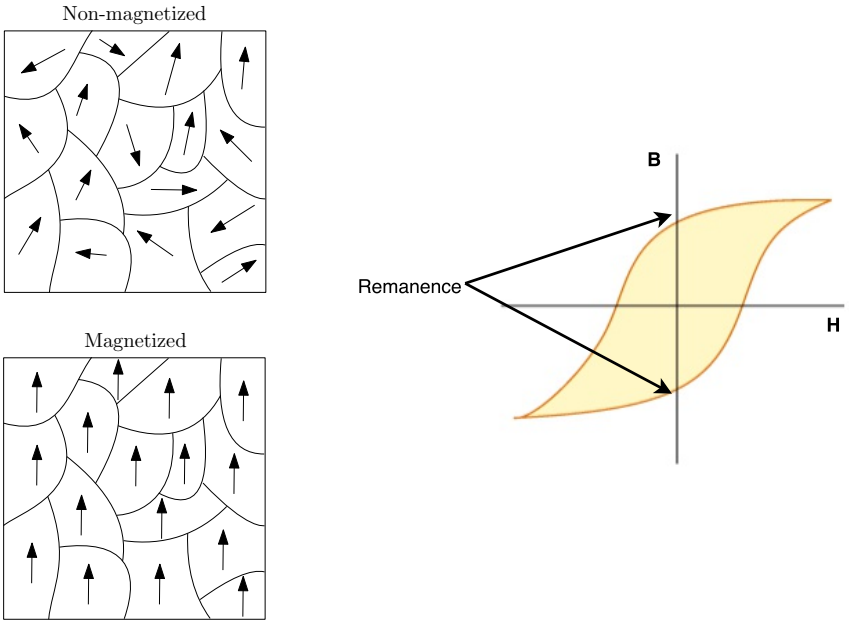

Figure 2.3: Visualization of the magnetic domains (left) and magnetic remanence (right).

Magnetic Self Inductance

The induced currents in an eddy current brake disc will, by Ampere's law, give rise to their own magnetic field that opposes the one that is applied. Wouterse [5] therefore suggests a hypothesis that when the relative speed between magnet and disc approaches infinity, the eddy current fields effectively cancel out the magnets resulting in a vanishing braking torque.

The Fringing Effect

As Figure 2.2 illustrates, effects of flux fringing is mostly seen in the air gap separating the poles in a magnet, the degree being dependent on the size of the gap, but it is also affected by the shape of the core and the winding technique[14]. The fringing is due to the differences in magnetic permeability of the core and the surrounding medium and causes the lines of flux to bulge outwards and leak into the surroundings. Larger and larger areas are affected as the distance between the poles increases, thus reducing the flux density in the air gap. According to McLyman [14] fringing is an important factor that should be taken into consideration when designing inductors, as it can cause many undesirable effects.

Electromagnets and Magnetic Hysteresis

Magnetic hysteresis is the phenomena when a ferromagnetic material retains magnetization **B** after an applied field **H** is turned off[2]. It is true for all such materials, though in different degrees. When magnetizing a ferromagnetic material one uses an external magnetic field to align the magnetic domains of the material. In a non-magnetized material, the direction of these domains are not aligned and their inner fields cancel each other out. By applying an external magnetic field the domains can be aligned, making the material magnetic. The time required for the domains to fully misalign themselves again depends on the properties of the specific material. The degree of retention at zero applied field intensity is called magnetic remanence, and this is visualized in Figure 2.3 along with the magnetic domains.

[2] H is also called the magnetic field intensity, and can be calculated as $H = Ni/l$, where N is the number of wire turns, i is the current and l is the length of the core. The magnetic flux density is known as $B = \mu H$, where μ is the magnetic permeability of the core material.

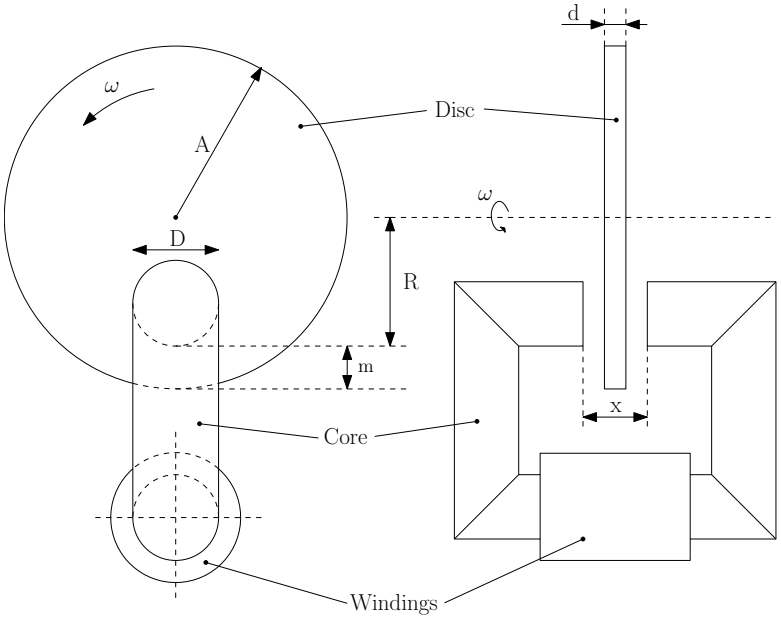

Figure 2.4: Illustration showing the system which Wouterse investigated [5].

2.3 Modeling Eddy Current Braking Torque

The mathematical foundation of analytical models to be presented is based on the assumption of a superconducting ring slipping over a non-magnetic and conductive material, which means that the return path of the eddy currents is constricted to the outer rim of the magnetic poles. Flux leakage outside the poles, i.e fringing, is therefore neglected. The validity of this assumption relies on the degree to which the disc thickness is larger than the pole diameter. Using this simplification, one way to find the braking power dissipation is to integrate the current density j under the pole projection area and multiplying it by the disc material's specific resistance ρ, i.e. $P = \rho j^2$, over the cylindrical volume of the disc under the pole projection area, $\pi D^2 d/4$. In accordance with Wouterse [5], this gives the braking power as:

$$P_{diss} = \frac{\pi}{4\rho} D^2 d B^2 v^2 \tag{2.6}$$

Here B is the magnetic induction in the air gap, D is the diameter of the poles, v is the linear speed of the disc and d is the disc thickness. Compensatory factors, c and α, has been introduced to deal with the discrepancies arising from the assumptions, as will be discussed in this section.

Smythe [1] was the first to model eddy currents on a rotating disk of a finite radius. In his work he specifically pointed out the demagnetizing effects that occur as a result of the eddy currents, effectively cancelling out the applied field at high speeds. In addition, he mentioned potential errors that could arise from resistivity change and buckling of the disc when heated from the braking action.

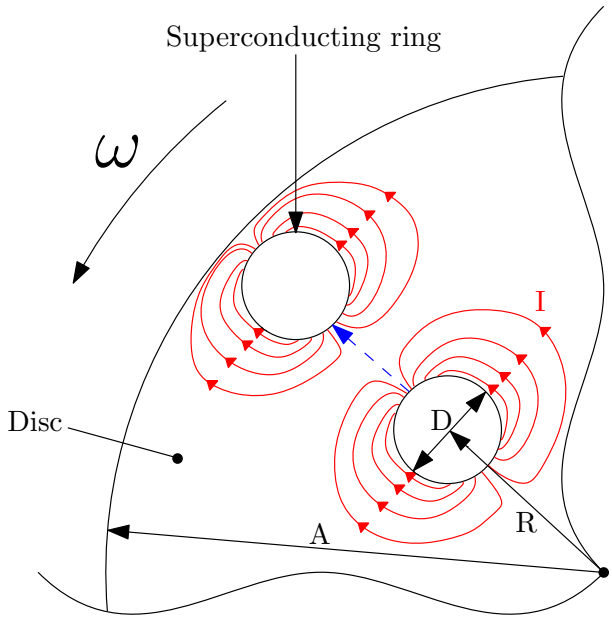

Figure 2.5: For infinite sheets the compensation factor c equals one half of the ideal model with a superconducting ring around the pole and decreases as the distance between the disc edge and pole is reduced. Though Wouterse [5] pointed out that it is of minor influence, the pole placement becomes a question of how much torque is gained by placing the pole at a larger radius, compared to the braking force loss resulting from coming closer to the disc edge.

Schieber [2] followed up on Smythe's work with a new comprehensive mathematical investigation of the system, re-evaluating the same problem. This resulted in a torque model that verified the one of Smythe while also expanding the theory so it became valid for linear motion.

Because of the induction effects Schieber [2] and Smythe [1] was restricted to the low speed, linear region. Wouterse [5] expanded the model into the high speed region, introducing an equation for finding the critical speed and the maximum generated force of an eddy current system, as the one seen in Figure 2.4. Below the critical speed, he proposed that the magnetic induction effects caused by the eddy currents was negligible compared to the original field B_0, and that the induction was almost perpendicular to the disc (i.e. no fringing). Wouterse's equation for the critical speed was given as:

$$v_c = \frac{2}{\mu_0}\sqrt{\frac{1}{c\xi}}\frac{\nu}{d}\sqrt{\frac{x}{D}} \tag{2.7}$$

Here D[mm] is the pole area diameter, μ_0[H m^{-1}] is the permeability of free space, x[mm] is the air gap between pole faces including the disc thickness d[mm], and ν[Ωm] is the specific resistance of the disc material. Wouterse estimated the parameter ξ as unity. The factor c includes the effects of the current return path under the pole hence making the model more accurate for real systems with discs

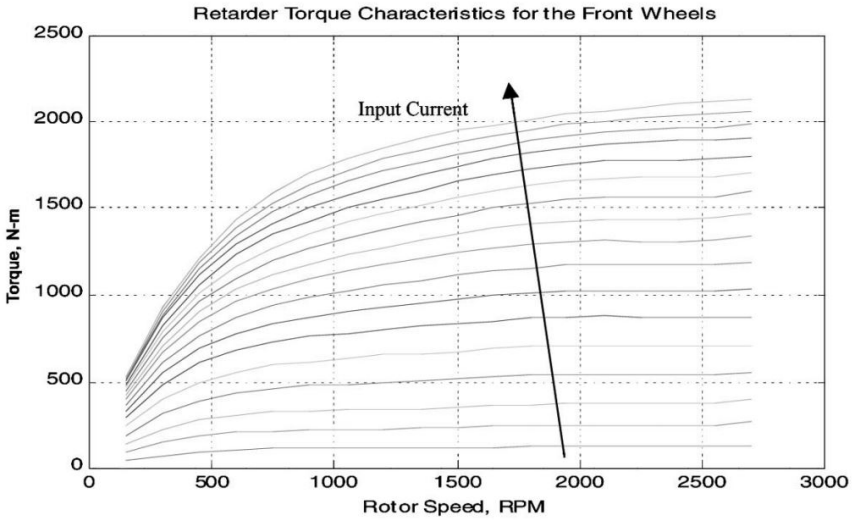

Figure 2.6: Torque vs rotor speed at different, constant, input currents[15]

of finite sizes and was, in agreement with Smythe [1] and Schieber [2], given as:

$$c = \frac{1}{2}\left[1 - \frac{1}{4}\frac{1}{(1+\frac{R}{A})^2(\frac{A-R}{D})^2}\right] \tag{2.8}$$

Here A is the disc diameter, R is the distance from the disc axis to the pole center, and D is the pole diameter. As the disc radius increases, the value of c converges to one half, and decreases as the pole location approaches the disc edge, as explained and illustrated in Figure 2.5.

The model in Wouterse [5] was later used by several others for the purpose of designing braking systems. Simeu and Georges [7] implemented a nonlinear control scheme for speed control, by deriving an approximate model (2.9) giving the brake force as a function of the exciting current and the angular speed:

$$f_b = (\alpha_0 + \alpha_1 i_e + \alpha_2 i_e^2)v \tag{2.9}$$

Here $\alpha_{0,1,2}$ were identified parameters. In order to approximate the B-H curve of the electromagnet, the following equation was used:

$$B = \begin{cases} B_r + \epsilon\mu_0 H & \text{for } H > 0 \\ -B_r + \epsilon\mu_0 H & \text{for } H < 0 \end{cases} \tag{2.10}$$

Here B_r and $\epsilon\mu_0$ represents the residual magnetic induction and the permeability of the material, respectively [7].

Based on the results of Simeu and Georges [7], Anwar [16] summarized the torque characteristics of an eddy current retarder[3]. Based on observations done at the

[3]A retarder is a device used in wide range of braking applications, primarilly heavy vehicles. As their working principle is based in electromagnetic induction, they can be modelled by the same basic principles.

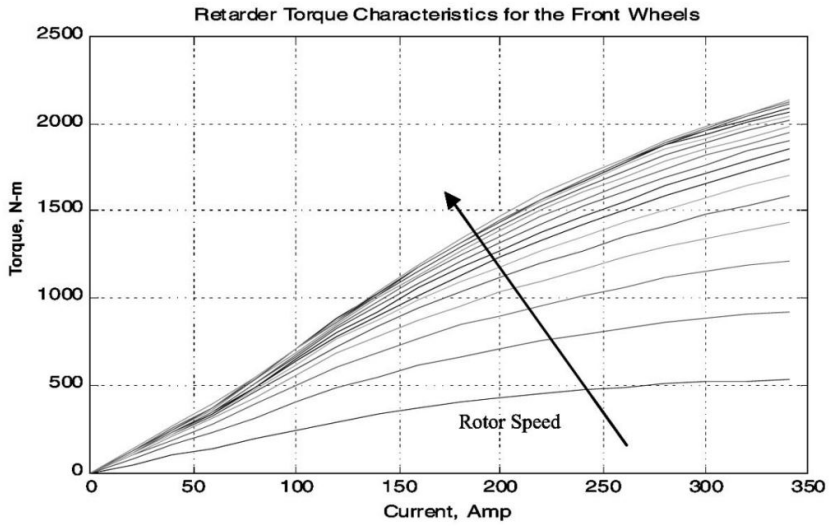

Figure 2.7: Torque vs input current at different, constant, rotor speeds[15]

Visteon Corporation he pointed out inaccuracies in assuming a linear relationship between the force or torque and rotor speed, as done in [7].

Performing a dynamometer test, the torque of a retarder was characterized at different speeds and input currents. In Figure 2.6 torque vs. speed is plotted at different input currents, while in Figure 2.7 current is varied while rotor speed is held constant. Anwar [15] claimed that these results disproved the assumption of Simeu and Georges [7] that the torque/speed behaviour is linear in the low speed region. Because of this, Anwar [15] proposed a parametric function that improved the torque-speed relationship through a quadratic function:

$$\tau(t) = f_0(\omega) + f_1(\omega)i + f_2^2(\omega)i^2 \tag{2.11}$$

Here,

$$f_i(\omega) = a_{i0} + a_{i1}\omega + a_{i2}\omega^2 \tag{2.12}$$

in which τ is the retarding torque, i is the current feedback from the retarder and $a_{i0,i1,i2}$ are identified parameters. Combining this function with the current response characteristics of the retarder (i.e. the electromagnet), Anwar [16] designed a closed loop control system primarily for motor vehicle applications.

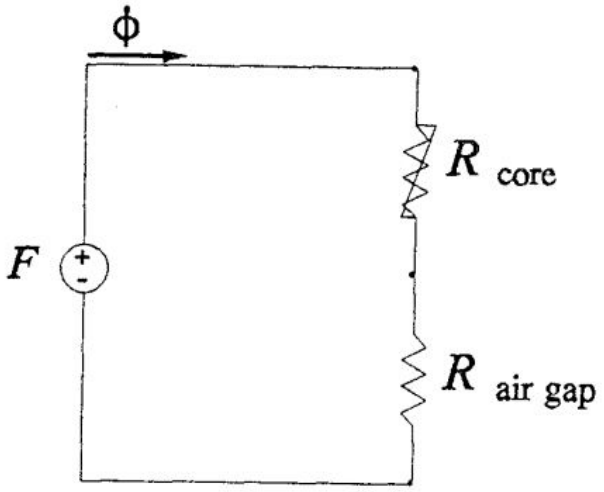

Figure 2.8: Magnetic circuit.
Magnetic circuit as modeled by Barnes et al. [8].

Barnes et al. [8] devised a computer model of a braking system for application in an exercise apparatus, which he based on the model arising from both Wouterse [5], Wiederick et al. [3] and Heald [4]. The model was based on a disc rotating in between two rectangular poles in the low speed region, calculating the magnetic field intensity B_0 by modeling the core as a magnetic circuit as seen in figure Figure 2.8. The model was given by:

$$F = abt\sigma B_0^2 \alpha c v \tag{2.13a}$$

Here,

$$\alpha = 1 - \frac{1}{2\pi}\left[4\arctan A + A\ln\left(1+\frac{1}{A^2}\right) - \frac{1}{A}\ln\left(1+A^2\right)\right] \tag{2.13b}$$

$$D = 2\sqrt{\frac{ba}{\pi}} \tag{2.13c}$$

Here, a and b are the cross sectional width and length of the core, respectively. A is the aspect ratio of the pole face and α is a factor that was introduced by Heald [4] to account for fringing effects.

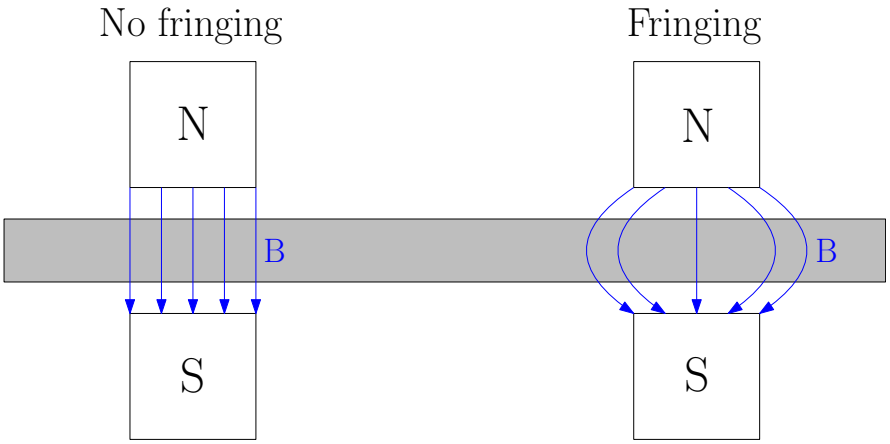

Figure 2.9: Neglecting fringing(left) and a more realistic model (right).

Gosline and Hayward [17], outlined the model of Wouterse [5] in order to design eddy current brakes for haptic interfaces. Because of its simplicity, this is the model on which the dimensioning and theoretical comparison done in this thesis was based on:

$$P_b = \frac{\pi\sigma}{4} D^2 d B^2 R^2 \dot{\theta}^2 \tag{2.14a}$$

$$\tau_b = \frac{P_b}{\dot{\theta}} = \frac{\pi\sigma}{4} D^2 d B^2 R^2 \dot{\theta} \tag{2.14b}$$

Here, P_b and τ_b are the braking power and the braking torque, respectively.

Chapter 3

The Eddy Current Braking Testbed

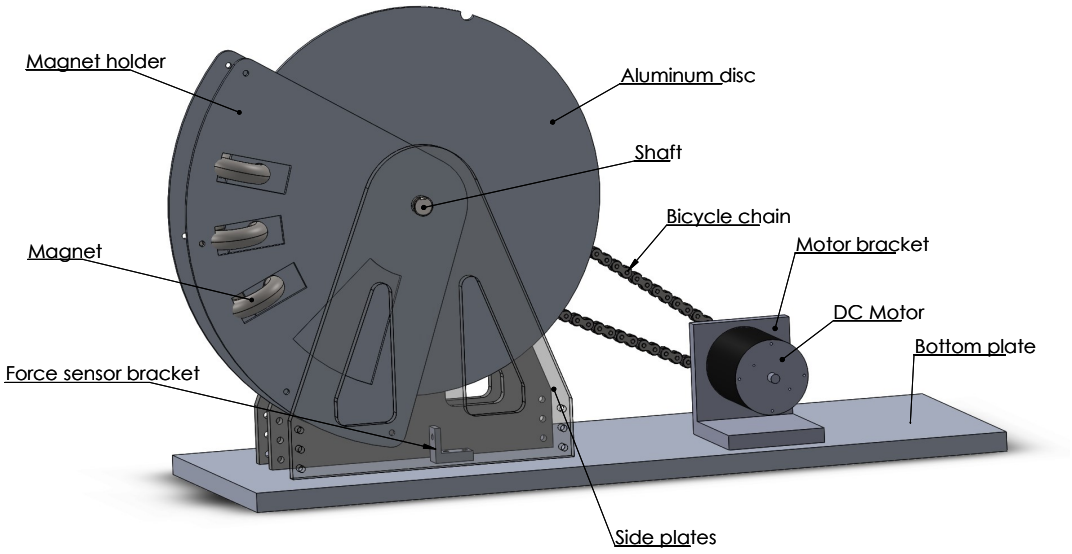

Figure 3.1: Conceptual CAD model of the ECBT, front view. The magnet holder and the disc rotates independently about the shaft, and upon braking the holder is pressed against the force sensor.

In order to validate the theoretical model presented in the previous section, along with the control scheme design, an eddy current braking testbed (ECBT) was designed and produced in collaboration with the workshop at the Department of Engineering Cybernetics at NTNU. Concept design, basic dimensioning, hardware implementation and other indicative information about the testbed's requirements was provided by the author. Final design was carried out by engineers in the workshop for manufacturing ease along with component availability and lead time.

Table 3.1: Model parameters of the eddy current braking testbed.

Parameter	Value
Disc radius, A	190 mm
Disc thickness, d	5 mm
Pole diameter, D	10 mm
Air gap (including disc thickness), l_g	5.2 mm
Number of turns, N	1200
Distance between disc axis and pole centre, R	185 mm
Conductivity of disc, σ	$2.0202 \times 10^7\,\mathrm{S\,m^{-1}}$
Specific resistance (resistivity) of disc, ν	$0.0495 \times 10^{-6}\,\Omega\mathrm{m}$
Permeability of air, μ_0	$1.2566 \times 10^{-6}\,\mathrm{H\,m^{-1}}$

3.1 Design and Dimensioning

3.1.1 Mechanics and Materials

The rotating, non-magnetic and conductive disc was designed with the maximum size feasible for the available lathe. The magnets were mounted on a large radius to give high torque while also being transferable to other systems with large rotors. Being easily available and cheap, aluminium 5052 was used as the disc material, with copper as a more conductive but expensive alternative. The conductivity of aluminium is highly sensitive in composition and thermal condition[18], factors which could cause inaccuracies in the eddy current brake model and should be taken into consideration during an experimental study. The accuracy of the ECB torque model depend upon the degree to which the pole diameter is larger than the disc thickness, i.e. $D > d$. At the same time, referring to equation Equation (2.14b), a larger disc thickness would increase the applied torque but would also require a higher current and/or number of windings to produce a sufficiently large magnetic field in the air gap. As further discussed in Section 3.1.2, the core of the electromagnets was of a circular cross section with a diameter of $D = 10\,\mathrm{mm}$. Being easily available in the workshop, a disc thickness of $d = 5\,\mathrm{mm}$ seemed to be a nice compromise and was therefore chosen. The magnets were fastened on a mount that could rotate independently about the same shaft as the disk. During braking this mount was pressed against a force sensor placed as indicated in Figure 3.1.

Using eddy current braking on exercise devices, more specifically stationary bicycles, is a case where electromagnets could play a key role in revolutionizing the way we interact with such equipment. Not only can it reduce maintenance, but also possibly produce faster resistance feedback to the user. An electrically controlled braking system could also result in better flexibility by means of creating a more comfortable adjustment process for the user. Rather than having to reach down between ones legs to adjust it mechanically, resistance could be adjusted almost instantly by the touch of a button. A testing range was therefore chosen

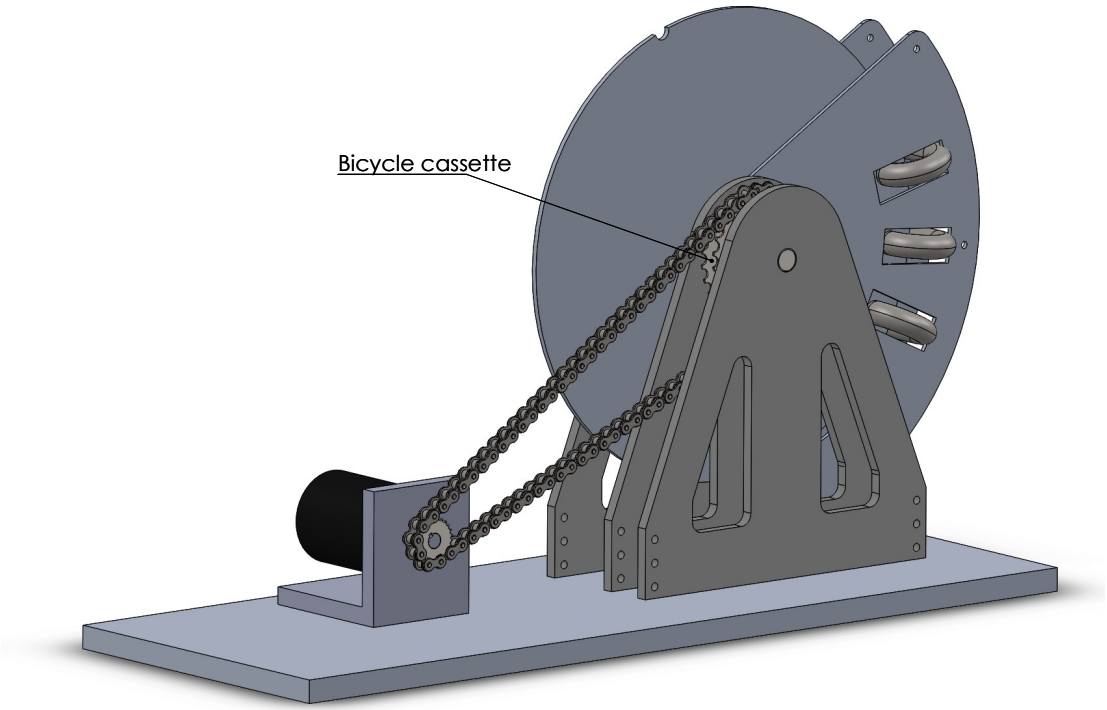

Figure 3.2: CAD model of the ECBT, rear view.

specifically with regards to exercise bicycles, in order to scale the system for such a use. In accordance with Lucía et al. [19] the speed range was chosen to be 60-100rpm which, along with a gear ratio of at least 1:3, corresponds to a disc speed of 180-300rpm. Testing within this range required a motor that was superior to the desired braking power. A bicycle cassette was mounted on the disc, giving the freedom to switch between different gear ratios. Transmission was done through a chain that was tightened by sliding and fastening the motor bracket along the base, accordingly.

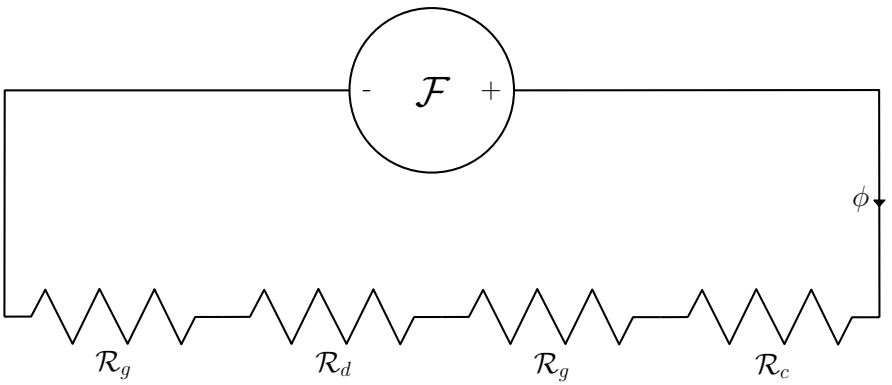

Figure 3.3: Idealized circuit equivalent of the electromagnetic system.

3.1.2 Electromagnet

Creating a Magnetic Flux Density Model

With Hopkinson's law (2.4) in Section 2.2.1, i.e. Ohm's law for magnetic circuits, the electromagnetic system was modelled as seen in Figure 3.3. The reluctance of the core, air gap and disc are respectively:

$$\mathcal{R}_c = \frac{l_c}{\mu_c A_c} \tag{3.1a}$$

$$\mathcal{R}_g = \frac{l_g}{\mu_g A_g} \tag{3.1b}$$

$$\mathcal{R}_d = \frac{l_d}{\mu_d A_d} \tag{3.1c}$$

Here μ, A and l represent the magnetic permeability, cross sectional area and length of the respective sections of the circuit. By noting the magnetomotive force, $\mathcal{F} = Ni$, where N is the number of windings and i is the current, the total magnetic flux was deduced as:

$$\phi = \frac{Ni}{\frac{l_c}{\mu_c A_c} + \frac{2l_g}{\mu_g A_g} + \frac{d}{\mu_d A_d}} \tag{3.2}$$

From 3.2, in agreement with Lee and Park [20], the reluctance of the core actually does not have any noticeable effect on the total reluctance of the circuit because, generally, $\mu_c >> \mu_g$. Hence, practically speaking, the core acts only as a flux channelling medium and only the width of the air gap, in addition to the number of wire turns and exciting current, determines the magnetic flux density in the gap. Using a non-magnetic material in the disc leads to the assumption that $\mu_0 \approx \mu_d$ which yields the model:

$$B_g = \frac{\phi}{A_g} = \frac{\mu_0 Ni}{2l_g + d} \tag{3.3}$$

3.3 gives the magnetic field density in the middle of a long solenoid, i.e. the core, assuming a constant winding radius and no fringing. The result can be derived by using Ampere's law and integrating the magnetic field resulting from each loop of wire along the winded length of the electromagnet. This is an idealized model and its accuracy will be discussed in Section 3.3.3.

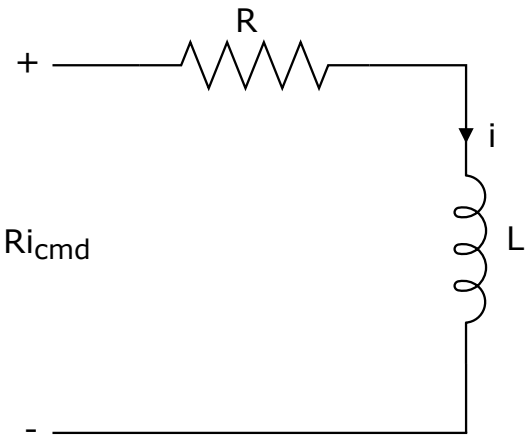

Figure 3.4: The RL circuit representing the electromagnet.

Current Response

An electromagnet can be modelled as an RL circuit as seen in Figure 3.4 with the command current i_{cmd} as the system input, as noted by Anwar [15]. Using Kirchhoff's voltage law yields the following first order differential equation for the exciting current, i:

$$\frac{di}{dt} = \frac{R}{L} i_{cmd} - \frac{R}{L} i \tag{3.4}$$

Here R is the total resistance of the RL-circuit, L is the total inductance and i_{cmd} is the command current. From (3.4) the time constant can be identified as:

$$\tau_i = \frac{L}{R} \tag{3.5}$$

The inductance L describes the inductors ability to oppose a change in current, and can be found from:

$$L = \frac{\mu_c N^2 A_c}{l_c} \tag{3.6}$$

Here μ_c is the core permeability, N is the number of windings, A_c is the cross sectional area of the core and l_c is the length of the core.
In order to keep the transient time small and hence minimize phase shift, it is desirable to reduce the inductance as much as possible. The magnets should therefore be connected in parallel:

$$\frac{1}{L_{tot}} = \frac{1}{L_1} + \frac{1}{L_2} + ... + \frac{1}{L_n} \tag{3.7}$$

Designing an ECB becomes a compromise between field density, magnet size, current frequency and power requirements. A fast response requires low inductance and/or higher coil resistance, which are two properties that contradict each other.

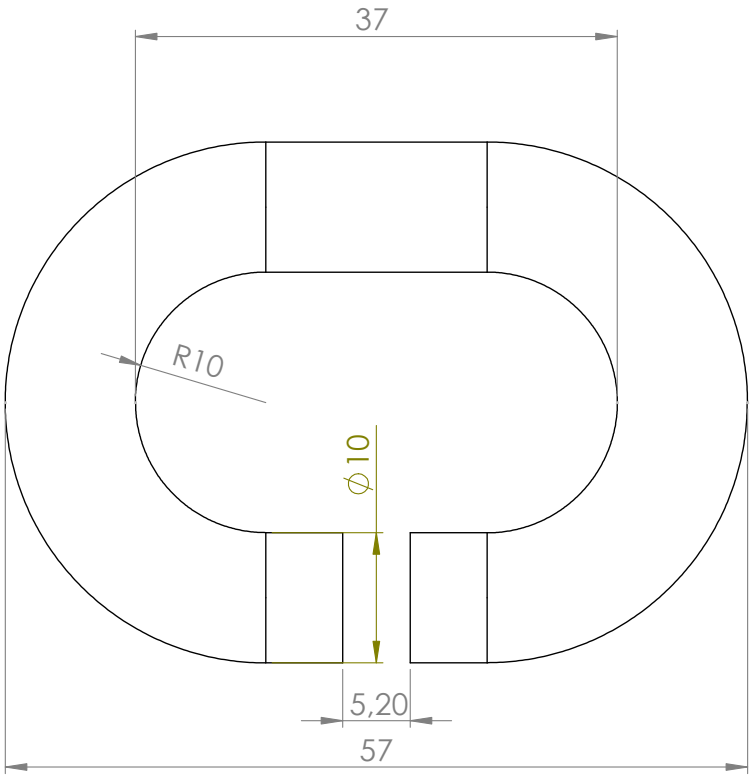

Figure 3.5: Core dimensions of the electromagnet.

Higher resistance can be obtained by adding more windings which in turn produces more inductance, and vice versa. Increasing input voltage will also reduce response time, the voltage being proportional to the slope of the current running through the coil. This is something that should be considered for the specific application.

Because of rather poor documentation and selection of off-the-shelf electromagnets the cores where designed in Solidworks by the author and thereafter crafted in the workshop, see Figure 3.5. Making them from scratch also gave insight into the design challenges of an application like this. The core was made out of soft iron, more specifically wrought iron, because of its superior properties with regards to magnetic remanence and linear relationship between magnetic field strength, H and field density B. This is why soft iron is the most popular choice for an electromagnetic core[21]. Choosing a material of low magnetic remanence becomes especially beneficial when it comes to applying time varying magnetic fields, as done by Karakoc et al. [12], and controlling torque, even though hysteresis effects can be overcome by using special kinds of control strategies as Simeu and Georges [7]. Soft iron is relatively free from other metal components, pure iron having a magnetic saturation limit of about 2T [22].

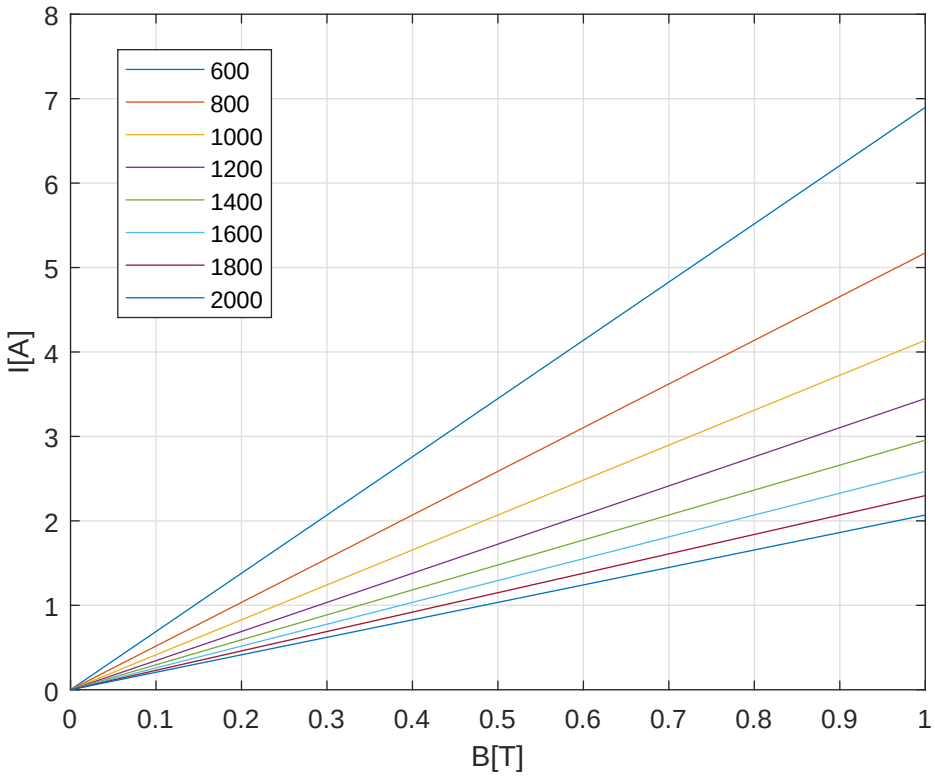

Figure 3.6: Required exciting current plotted against the magnetic field with different number of windings.

A power range of 50-150 W was chosen because of its relevance to cycling, the higher range being constricted to the lower cadence zones. For benchmarking with cycling as an application the system was designed to be able to generate 150 W of braking power at 180 rpm, theoretically, according to the model presented in Section 2.3. One limiting factor was the available core size which was of a diameter of D =10 mm, another was the length of the air gap which was constricted to the thickness of the disc plus clearance between the disc and the pole of the magnets. Setting the clearance to 0.1 mm gave an air gap of $l_g = 5.2$ mm, being relatively small while at the same time giving room for some small vibrations and inaccuracies in the system. The magnetic field, B, could be varied with the applied current and/or number of windings. Figure 3.6 shows the theoretic magnetic field intensity in the air gap vs. the applied current with different number of windings, using (3.3). Either a great number of turns was needed - leading to a bulky device and a larger time constant in the resulting inductor, or a large current - which increased power supply demands and gave more power dissipation in the spool, producing heat and possibly the need for cooling.

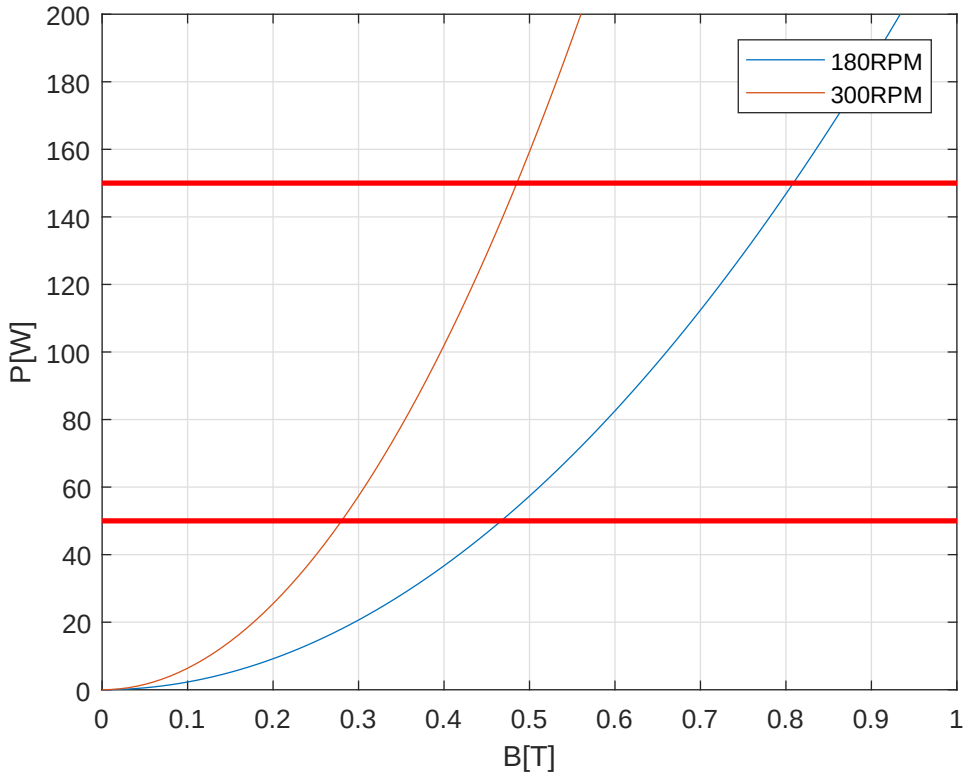

Figure 3.7: The theoretical braking power vs. the applied magnetic field at the chosen upper and lower speed, for the given configuration with parameters from Table 3.1.

Figure 3.7 shows the theoretical power output of an electromagnetic brake with the parameters of Table 3.1 and predicted braking power by using the model from (2.14a), with three poles. The horizontal lines indicate the power output range that the eddy current brake should be able to generate. The required number of turns was calculated with a current of 3 A through each magnet. As mentioned, the brake was designed to generate a maximum braking power output of 150 W in the entire speed range, with a required magnetic field strength of just above 0.8 T at 180 rpm. Using (3.3), this gave the following number of turns:

$$N = \frac{Bl_g}{I\mu_0} = \frac{0.8T \cdot 5.2 \cdot 10^{-3}m}{3A \cdot 1.2566 \cdot 10^{-6}\frac{H}{m}} \approx 1104 \tag{3.8}$$

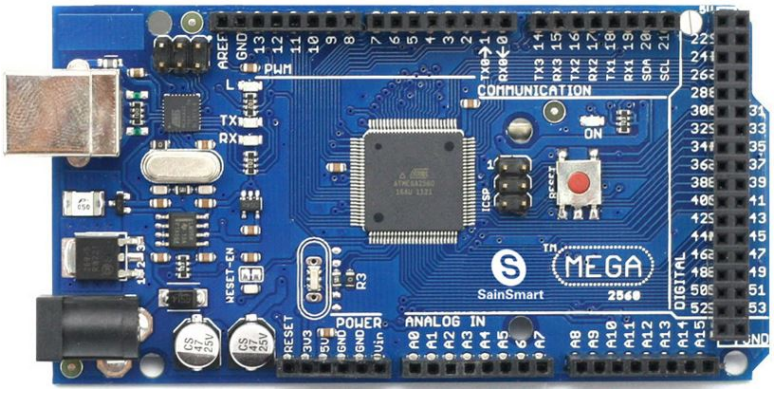

Figure 3.8: Arduino Mega2560

Table 3.2: Parameters of the Arduino Mega 2560.

Parameter	Value
Operating Voltage	5 V
Digital I/O pins	54
Analog Input Pins	16
Clock Speed	16 MHz
Flash Memory	256 kB
SRAM	8 kB
EEPROM	4 kB
ADC resolution	10 bit

3.2 Hardware and Communication

3.2.1 Microcontroller

Data aquisition (DAQ) and control was done by using a cloned microcontroller of the type Arduino Mega 2560, as seen in Figure 3.8. This is a low-cost device that has proven to be a reliable platform, even for lab applications [23]. It is based on the ATmega2560 processor. The device has a 10bit analog to digital converter (ADC) and 15 of the digital I/O pins can be used for pulse width modulation (PWM). An Arduino Uno was used at first, but proved to have insufficient memory as the system grew. The parameters of the microcontroller are seen in Table 3.2.

3.2.2 Software

The Matlab and Simulink support packages for Arduino were used to communicate with the hardware. With these packages, communication could be done in two ways - either programatically in Matlab or with the use of Simulink models. In both cases a server is set up on the Arduino, enabling communication back and forth. When using Matlab this server responds to commands sent from the command window or a script, meaning the code runs on the computer. In the latter

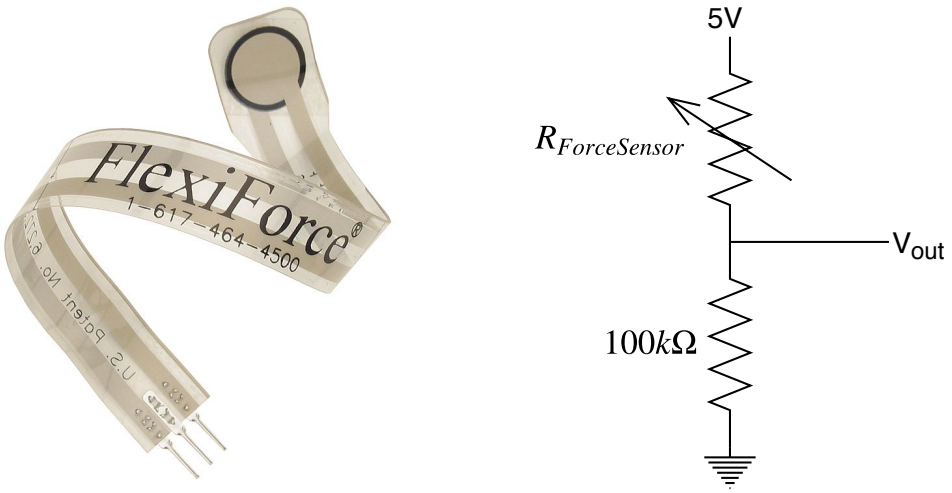

Figure 3.9: The Tekscan FlexiForce A201-25 piezoresistive force sensor(left) and the implemented voltage divider circuit(right).

case the model is converted into code that runs directly on the microcontroller [24]. Among many other things, the library has Simulink blocks for configuring and accessing the Arduino's inputs and outputs. It is also possible to deploy the model for standalone operation on the board without a computer connection, and it has an 'External Mode' which enables you to interactively monitor signals and tune parameters while the model is running on the device. This proved to be very convenient during the testing and implementation process.

3.2.3 Measuring Braking Torque

A capacitive force sensor from SingleTact was originally planned for measuring the braking force. After having some issues with this sensor due to heavy nonlinearities, a piezoresistive[1] force sensor, the FlexiForce A201-25 from Tekscan, was obtained and implemented. In practice the sensor acts as a variable resistor and can measure forces up to 20lbs, having a resistance that is inversely proportional to the force applied. The sensor was implemented with a simple voltage divider circuit, seen in Figure 3.9. The voltage output of this circuit can be calculated as:

$$V_{out} = \frac{100k\Omega}{R_{ForceSensor} + 100k\Omega} \cdot 5V \tag{3.9}$$

[1]The word 'Piezo' is derived from Greek and means to 'press' or 'squeeze'. Piezoresistive sensors exploit the fact that some materials change their electrical resistance when acted upon by a force.

3.2.4 Motor Control

Figure 3.10: RE50 200W DC motor from Maxon Motors [25].

Table 3.3: Motor and Encoder Specifications at 24V

Parameter	**Value**
Nominal Speed	5680 rpm
Nominal torque	405 mNm
Speed Constant	248 rpm V^{-1}
Torque Constant	38.8 mNm A^{-1}
Resolution	500 turns^{-1}
Max Operating frequency	100 kHz

An RE50 200W graphite brushed DC motor fitted with an HEDL5540 encoder, both from Maxon Motors, was used together with a discrete PI controller to drive the motor. Specifications are seen in Table 3.3.

3.3 Implementation

3.3.1 Spinning the Disc

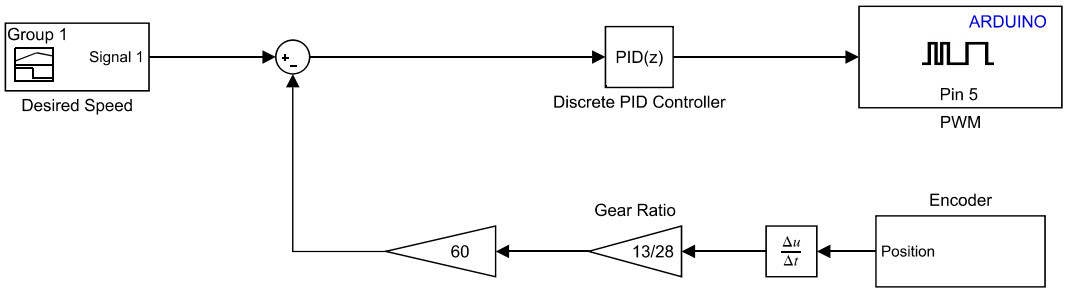

Figure 3.11: A Simulink block diagram of the motor control system.

The encoder was implemented in Simulink via a device driver block[2] based on examples from MathWorks File Exchange [28]. The freewheel mechanism due to the bicycle cassette and the force sensing system meant the motor only needed to be driven in one direction. This simplified the need for an advanced motor controller chip. An H-bridge hobby component chip from Robotshop.com was originally tested but proved to be more of an unnecessary source of error than a convenience, because of jitter issues. Instead, a MOSFET[3] of the type IRLZ44N was used as a relay along with a 500 Hz pulse-width modulated signal from the Arduino to control the motor current. IRLZ44N is a fast switching logic gate drive MOSFET, which meant that it could be directly driven by the Arduinos output signal. Rated for a continuous drain current of 47 A and a maximum drain-source voltage of 55 V, the MOSFET seemed suitable for a high power application such as this. Heatsinks were not fitted, but operating temperature was carefully monitored while the system was running. Switching the current also meant less heating of the MOSFET.

The encoders' motor shaft position was differentiated, scaled according to the chosen gear ratio and converted to revolutions per minute. The highest ratio, $n_{disc}/n_{motor} = 13/28$, gave the most torque while also providing the speed needed and was thus used through the entire experiment. An Arduino PWM block was connected to the output of a discrete PI-controller with a saturation limit of 255, giving 100% duty cycle when reached. A signal builder block gave a convenient way of designing custom desired speed inputs, as seen in Figure 3.11.

[2]Device drivers can be made by using S-functions, to generate custom designed code that runs on the microcontroller [26][27].

[3]MOSFET = Metal-Oxide-Semiconductor Field-Effect-Transistor

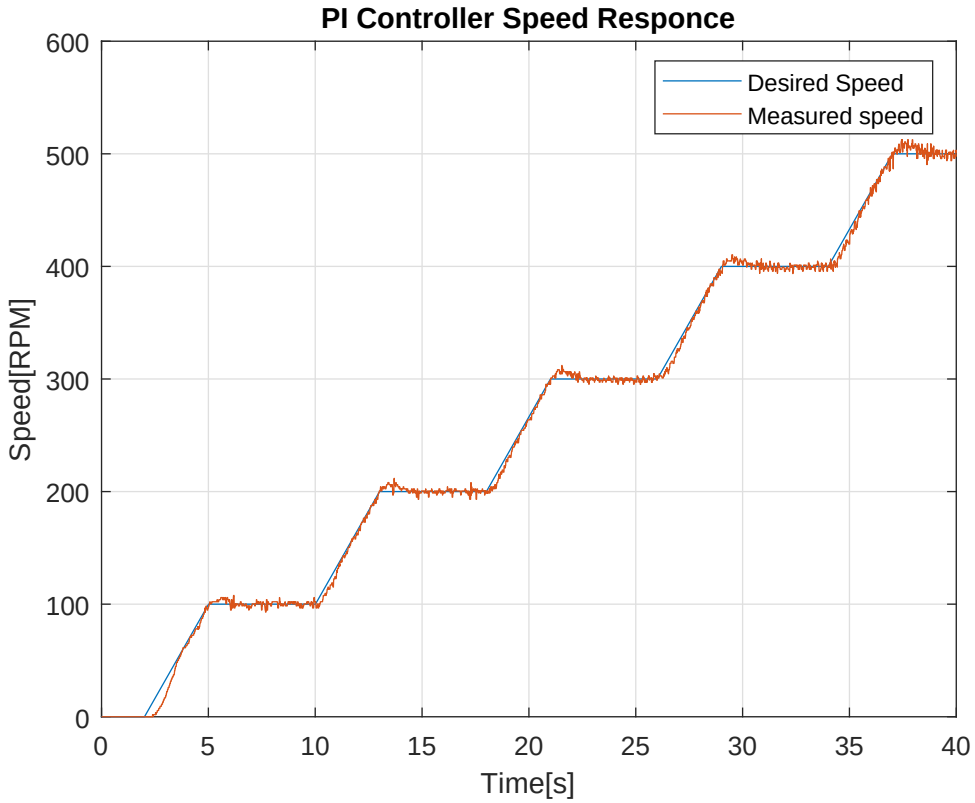

Figure 3.12: Responce plot of the PI controller with the parameters $K_p = 0.5$ and $K_i = 1.2$.

PI[4] control is a highly robust control method that computes the system input based on the difference between the measured and the desired state of the system. The input is given by:

$$u(t) = K_p e(t) + K_i \int_0^t e(t')dt' \tag{3.10}$$

Here the parameters K_p and K_i are parameters that can be tuned for the desired controller response and $e(t)$ is the regulation error. The proportional term, as the name implies, computes an input proportional to the error but also cannot always compensate for steady state errors. The integral part compensates for this by integrating the error and scaling it by the factor K_i, adding to the proportional term and increasing the input $u(t)$ as long as the error stays non-zero. A derivative term, $K_d \frac{de(t)}{dt}$, can be added for more control over the settling of the system. This term depends upon the rate of change of the error, and as the error gets smaller the D-part reduces the system input which can be used to reduce settling time and overshoots.

Discrete controllers must be used when dealing with digital signals as in the

[4]P = Proportional, I = Integral

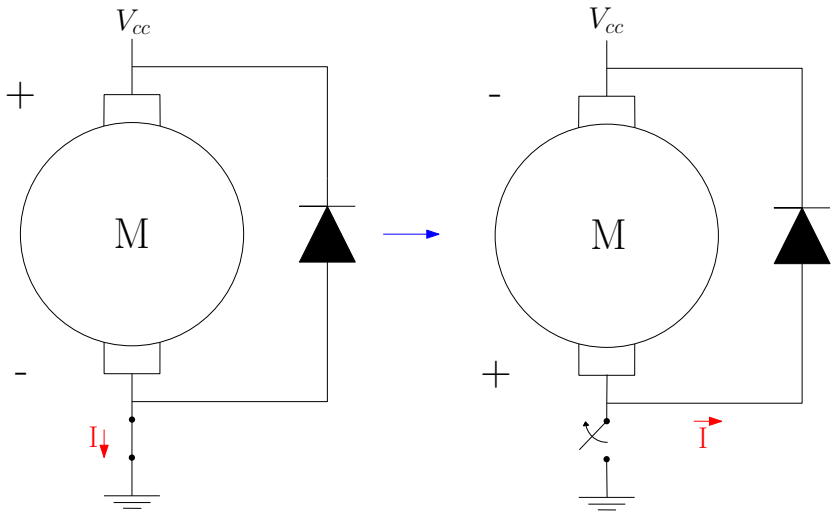

Figure 3.13: A flyback diode enabled the current to dissipate safely after the switch was opened.

ECBT, as opposed to analog systems with continuous signals. The applied PI controller used a Forward Euler integrator method to perform discrete-time integration of the error, with a sample time of 0.01 s.

Due to the freewheel mechanism the controller input was designed as a ramp rather than a step response. If not, because of the discs ability to spin faster than the motor, the acceleration of the disc easily caused large overshoots and resulted in instability. These overshoots could also have been avoided by choosing small controller gains, but in order to keep the disc spinning at a constant velocity when applying braking torque, response time had to be quick and this solution proved to be a nice compromise.

When switching inductive loads, such as motors, it is important to protect the circuit from large voltage spikes that can occur when the transistor switches off. The equation for the voltage across an inductor, $V = L\frac{di}{dt}$, says that the voltage is dependent on the rate of change of the current running through the inductor. Switching off the transistor effectively pushes this current slope towards negative infinity and as a result the voltage rises to a level where the current can discharge to a nearby conductor, often damaging the transistor and causing sparks across the pins. This was avoided by adding a diode, also known as a *snubber*, *flyback* or *kickback* diode, across the input terminals of the motor as seen in Figure 3.13. As the inductor, i.e. motor, resists the drop in current the resulting voltage across it will be of opposite polarity than before the switch, and the diode will start to conduct. In this way the voltage spikes can be nearly eliminated as the current is allowed to be dissipated as heat in the inductor. The same principle was implemented with the magnets. High pitch noise resulting from the PWM signal was reduced by adding a small ceramic capacitor across the terminals. The schematics of the system can be seen in the overview in Section 3.3.8.

3.3.2 Equipment

(a) DSO Shell Digital Oscilloscope.

(b) UNI-T UT132E multimeter.

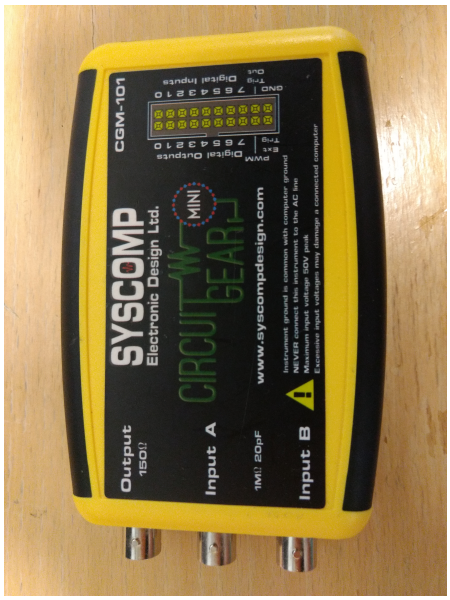

(c) Circuit Gear Mini (CGM-101).

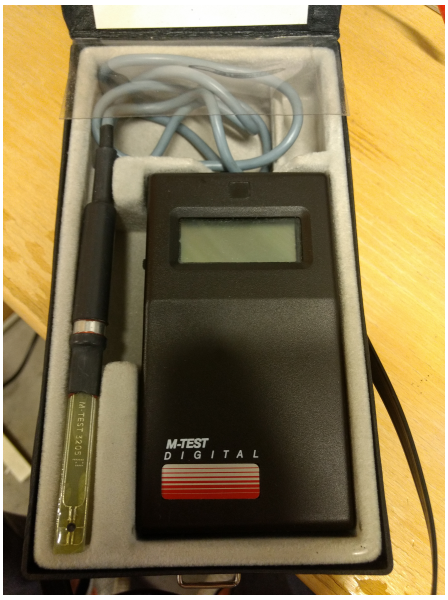

(d) Gaussmeter from Mauer Magnetic.

Figure 3.14: Measuring equipment used during implementation.

The DSO Shell (Figure 3.14a) and the CGM-101 (Figure 3.14c) oscilloscopes proved to be very useful in troubleshooting and testing the outputs of the Arduino before running the full system. The DSO was mainly used to monitor the PWM outputs controlling the magnets and motor, ensuring that the controller was not active before turning on the external power supplies. If not, the large starting current of the motor risked damaging the circuit and putting a large strain on the mechanics in addition to causing instability in the motor control

Figure 3.15: The home-made magnet with approximately 1200 windings, wrapped in heat resistant Kapton and electrical tape.

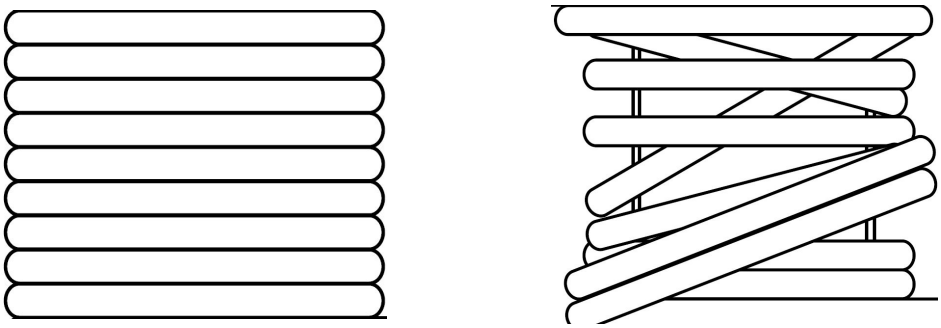

Figure 3.16: An even winding technique (left) is desired but more difficult to obtain. An uneven winding technique (right) produces more fringing [14].

system. The CGM-101 from Syscomp, with its ability to do real time spectrum analysis (FFT), was used to validate the PWM frequency of the Arduino and measure mechanical noise.

3.3.3 Creating a Magnetic Field

The amount of turns, current and the core length clearly reduced the viability of (3.8) because of the relative difference in radius between the inner and outer windings. The equation assumes straight field lines between the poles, something that is not true when having such a large air gap, referring to Section 2.2.2. It also assumes a constant field through the length of the core, which is not true because of the difficulties of winding the layers evenly by hand. This uneven winding technique is a significant cause of fringing, according to McLyman [14]. Redesigning the magnets was not considered an option and they were implemented with the rather inaccurate theoretical foundation as they were, being a potential source

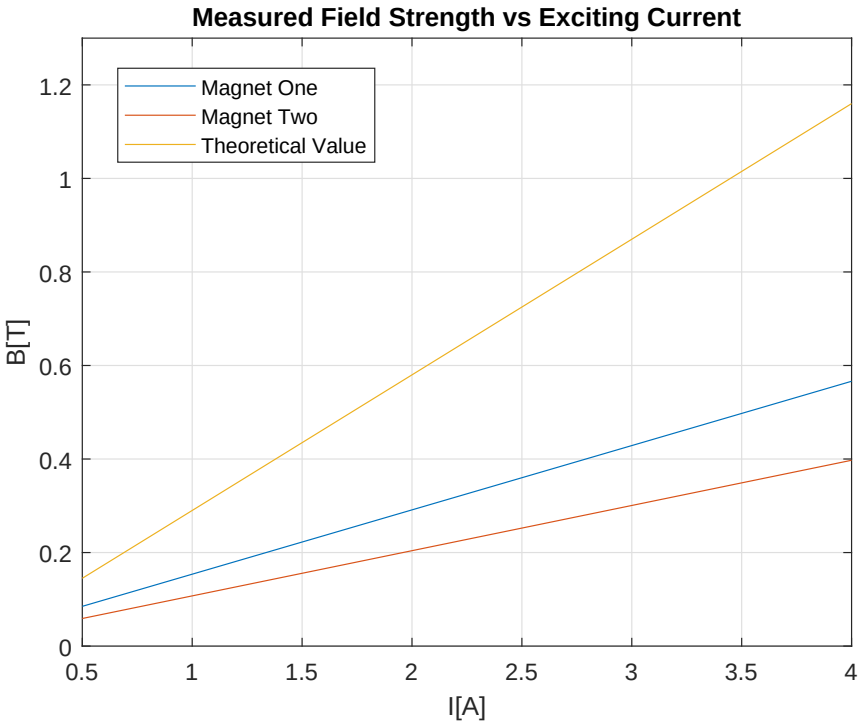

Figure 3.17: The measured field of the electromagnets differed both from each other and from theoretical values calculated from Equation (3.3), as could be expected because of the deviations from the idealized model. Theoretical deviations of about 50% and 67% were seen in magnet one and two, respectively.

of error for the systems' dimensioning. Figure 3.15 shows one of the magnets, and Figure 3.16 illustrates the difference between an even and uneven winding technique.

As initially planned, three magnets were made but one was damaged during wiring and proved to be difficult to mount without coming in contact with the disc. Fastening of the magnets was done by the use of a relatively heat resistant glue. For proof of concept, two magnets were therefore used during experimentation. Figure 3.17 shows large differences between theoretical and measured magnetic field density values for both the magnets that were used. Their electrical resistance were measured to be the same, $4.2\,\Omega$, at room temperature by the use of a multimeter, indicating that roughly the same number of windings had indeed been put on each of them. Their difference in magnetic properties were therefore thought to be due to fringing effects caused by an uneven winding technique. This most likely resulted in a non-uniform field through the length of the core, something that could also have contributed to the theoretical deviations. According to McLyman [14] fringing flux can cause hotspots in the windings, which was observed on the magnets.

3.3.4 Collecting Data

As mentioned in Section 3.2.2 data was collected by the use of the Arduino Simulink Package, each analog pin having a theoretical maximum sampling rate of 10 kHz according to the documentation[29]. However such a high rate was not obtained, possibly because of underlying delays caused by the serial communication with the board, plotting each output and sending the data to workspace in Matlab. Higher sampling rates proved unstable, suddenly freezing and skipping large amounts of samples. This could also have been caused by limitations in the PC that was used, a Samsung laptop with a 1.8 GHz Intel i5 processor and 8 GB of RAM, even though CPU usage was not considered to be the issue after monitoring it during testing. A rate as low as 100Hz was found to give reliably stable readings and allowed signals to be visualized in real time. For proof of concept and given the systems nature a higher sampling rate was considered unnecessary, but limited the frequency of braking torque variation. Nyquist's sampling theorem says that the sampling frequency should be at least double that of the highest signal frequency that is to be measured in order to avoid aliasing, i.e. $f_{sampling} > 2f_{signal}$. This means that a sampling rate of 100 Hz can only accurately reproduce signals with frequencies up to 50 Hz.

3.3.5 Calibrating the Force Sensor

Finding the Input/Output Relation

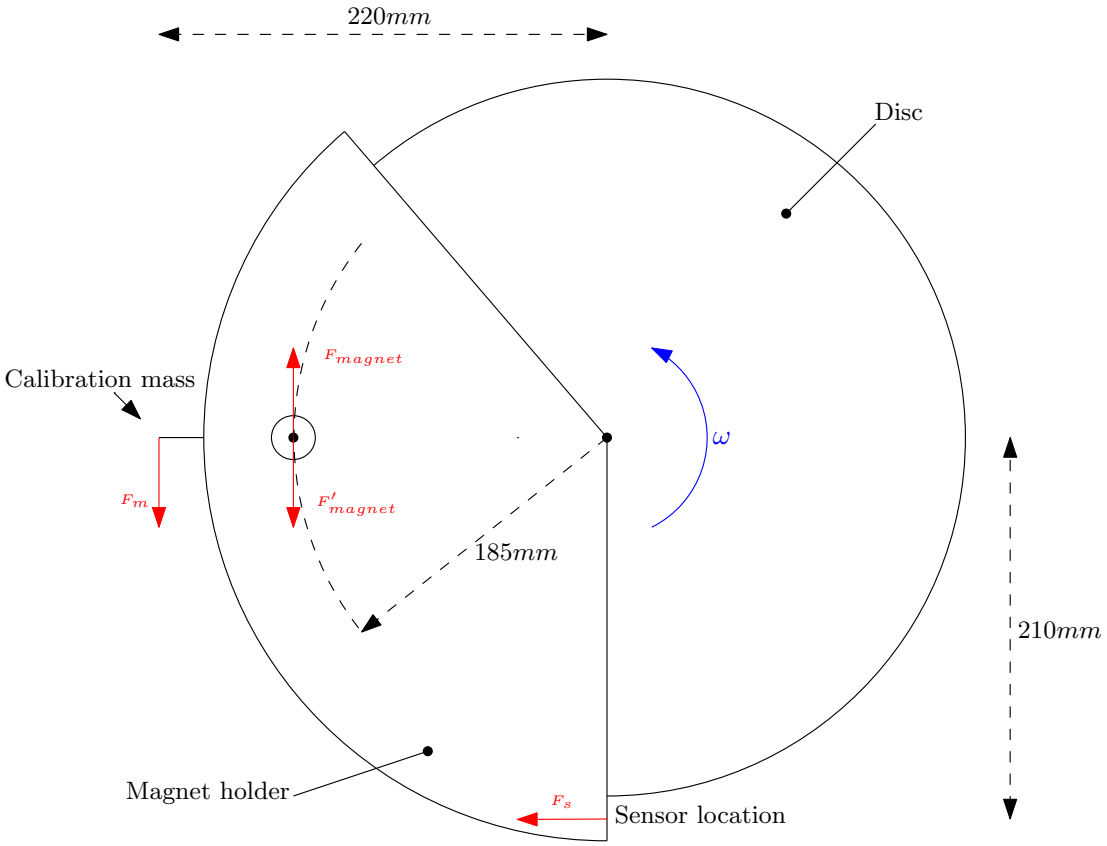

Figure 3.18: Calibrating the sensor with known weights.

Calibration was done by mounting the force sensor onto the ECBT and hanging known weights from a screw mounted on a horizontal line from the disc axis on the magnet holder. This simulated an equivalent braking force from input to output, as indicated in Figure 3.18. Calibrating the sensor after mounting it on the ECBT ensured that the calibration mass was equally distributed on the sensor at each test. Output was measured with the help of a Simulink model running on the Arduino. The initial value, i.e. the output due to the weight of the magnet holder, was stored at the start of each test to help minimize effects of sensor drifting, as further discussed in Section 3.3.5 and Section 6.1.1. Storing the value was done by having a switch route the initial ADC output into a 'Sample and Hold'-block. The block was triggered by the rising edge at a set time instant and stored the value for the rest of the program, implemented as seen in Figure 3.19.

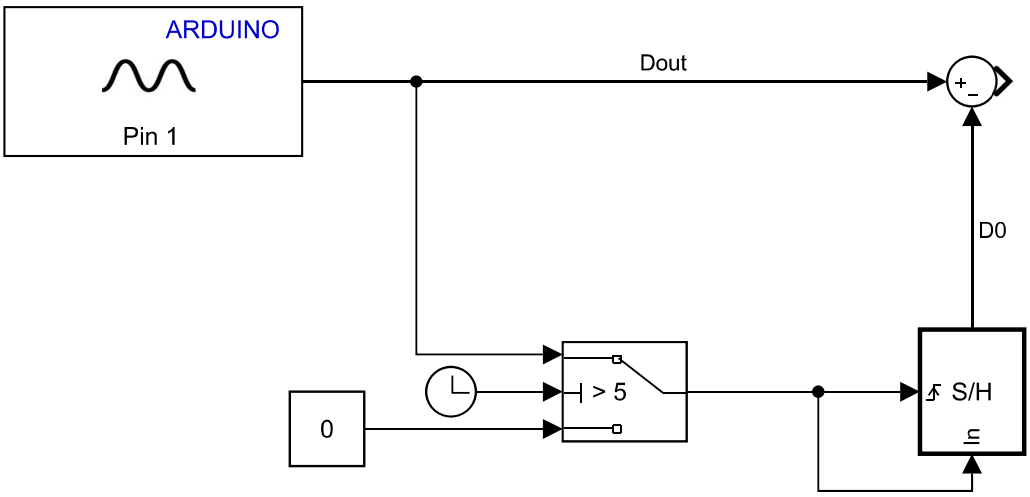

Figure 3.19: Storing and subtracting the weight of the magnet holder at the start of the program.

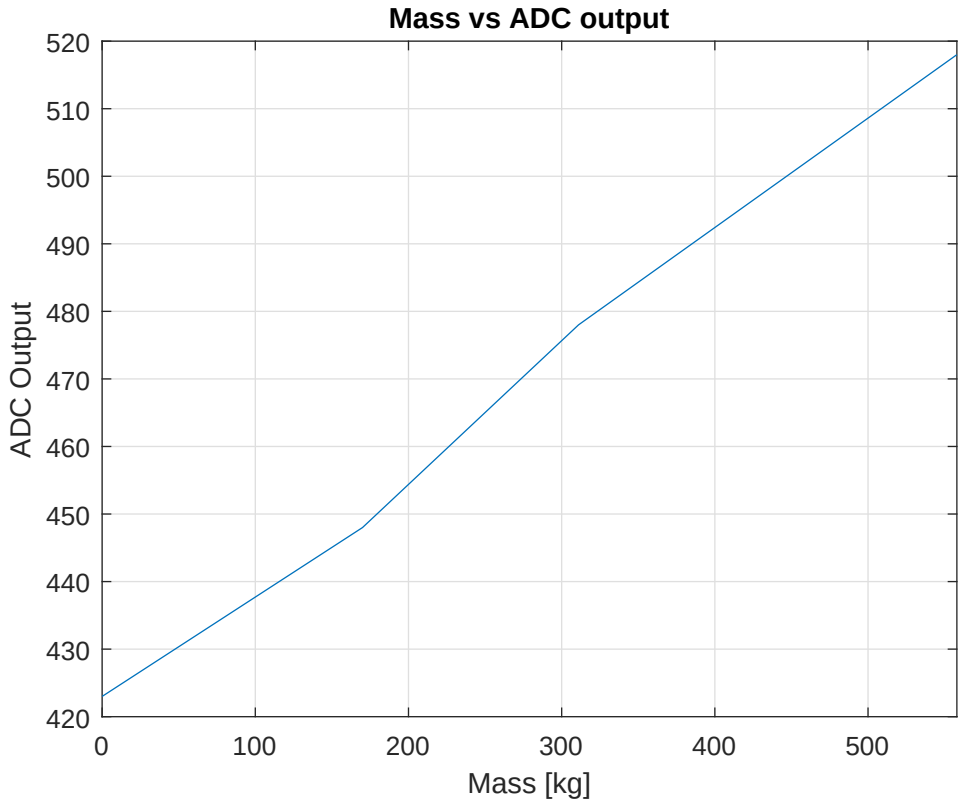

Figure 3.20: The relationship between applied mass and digital output shows good linearity.

The slope was found by loading the magnet holder with different weights and noting the corresponding ADC output. The masses were verified by a kitchen scale to be 170 g, 311 g and 558 g, having an equivalent mass at the sensor location of 177 g, 326 g and 585 g. The output of the ADC can be seen in figure Figure 3.20.

The slope of the mass-output relationship at the sensors location was found to be:

$$\frac{\Delta m}{\Delta D_{out}} = \frac{m - m_0}{D(585g) - D_0} = \frac{0.585kg}{518 - 423} = 6.2 \cdot 10^{-3} \frac{kg}{D_{out}} \tag{3.11}$$

Here D_{out} is the output from the ADC. This gave the braking force:

$$F_s = 6.2 \cdot 10^{-3} \frac{kg}{D_{out}} \left(D_{out} - D_0\right) \tag{3.12}$$

Here D_0 is the initial value, the ADC output in response to the weight of the magnet holder, stored by the 'Sample and Hold'- block. The total torque from the magnets could then be calculated as:

$$\tau = \frac{210}{185} \cdot 0.185m \cdot F_s \tag{3.13}$$

Ideally, this would give a minimum detectable change in torque, i.e. resolution, of:

$$\tau_{res} = 6.2 \cdot 10^{-3} kg \cdot 9.81 \frac{m}{s^2} \cdot 0.185m = 0.0113Nm \tag{3.14}$$

Handling Unstable Voltage References

Sensor drifting and inconsistent readings lead to the discovery that the Arduinos output voltage was not stable as readings between 4.7 and 5 V were obtained using a multimeter. The problem was addressed by using an external, stable, 5 V power supply to power the rails of the breadboard leaving the Arduinos voltage output separate from the connected hardware. In addition, to also ensure a stable ADC reference, voltage was provided from the 5 V power rail through a resistor connected to the Arduinos AREF pin and the reference voltage was configured to be external through Simulink[5]. This would not have been necessary had the supply voltage and ADC reference voltage varied the same, considering the ratiometric[6] properties of the force sensor. According to documentation[30] the AREF pin should be connected to a 32 kΩ resistor going to ground, making it a voltage divider circuit. Calculations showed that this clearly was not the case, as the voltage was measured to be 2.37 V between AREF and GND on the Arduino when using only a 1 kΩ resistor. This highlights the importance of measurement and using the documentation only as an indicator when dealing with low-cost

[5]When using an external reference it is important to configure this programatically before trying to read an analog input, to avoid shorting the AREF pin with the internal reference voltage[30].

[6]The output of a ratiometric sensor is directly proportional to its supply voltage.

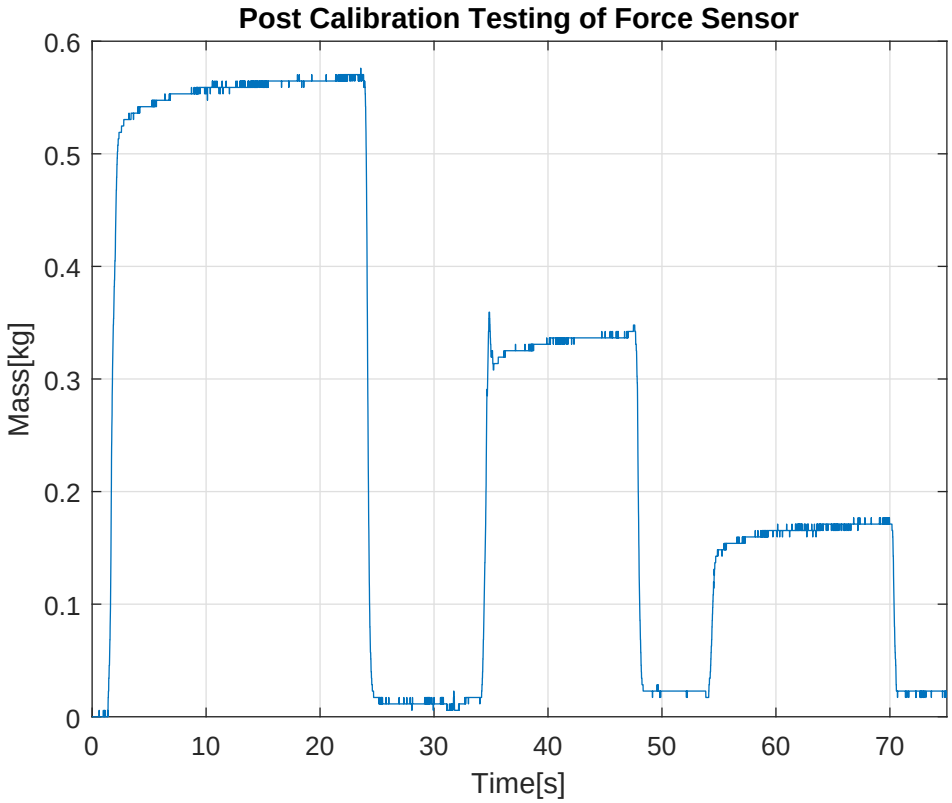

Figure 3.21: This plot shows the measured mass, as indicated in Figure 3.18 after calibration and with a stable reference voltage. The accuracy of the measurements are presented in Table 3.4.

Calibration Mass [g]	Measured Mass [g]	Error [%]
170	171	+0.6
311	336	+7.4
558	565	+1.2

Table 3.4: Mass readings were taken from the last few seconds of each peak to ensure the most accurate result.

hobby components, especially non-original hardware as the specific Arduino board used here. Post-calibration force sensor outputs can be seen in Figure 3.21 and Table 3.4.

3.3.6 Dealing with Noise

Noise was measured with the use of the CGM-101 oscilloscope, by scoping V_{out} as seen in Figure 3.9 at speeds from 100-500 rpm. The noise was believed to be a result of a non-straight shaft or disc in addition to some looseness in the bicycle cassette bearing, causing vibrations that affected the magnet holder and hence the force sensor, in addition to disturbances from the PWM signal running the

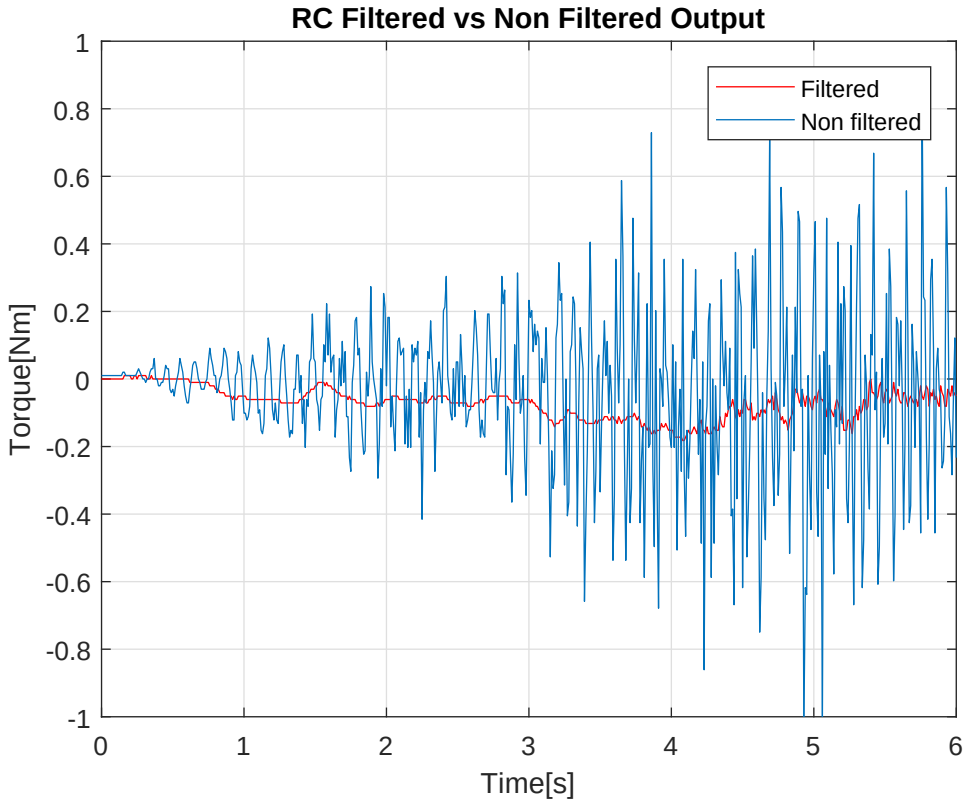

Figure 3.22: A test from zero to 500RPM showed the RC filter doing its job but also revealed some sensor drifting when accelerating.

Speed[RPM]	Noise [Hz]
100	5
200	30
300	70
400	100
500	106

Table 3.5: Measured mechanical noise frequency at different speeds.

motor. Studies have actually shown that the Tekscan Flexiforce sensor has more noise than other sensors in the same category [31], something that will be further discussed in Section 6.1.1.

The looseness in the bearing also caused sporadic movement in the chain that eventually lead to instability and the sprocket actually failing to grasp the chain properly. The noise problem was dealt with in two ways; an RC filter was designed to remove the noise arising from the shafts/disks distortions and a chain tightening mechanism was made in order to dampen the chains fluctuations.

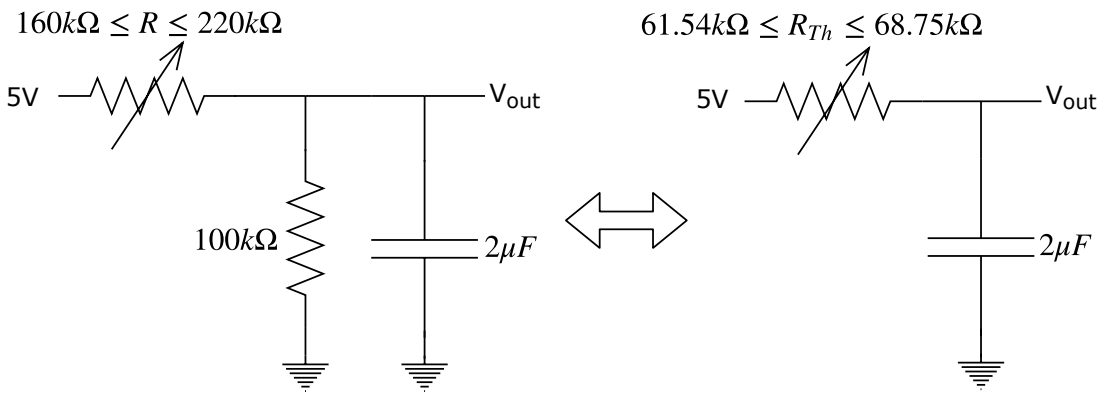

Figure 3.23: RC filter circuit (left) and its Thevenin equivalent(right).

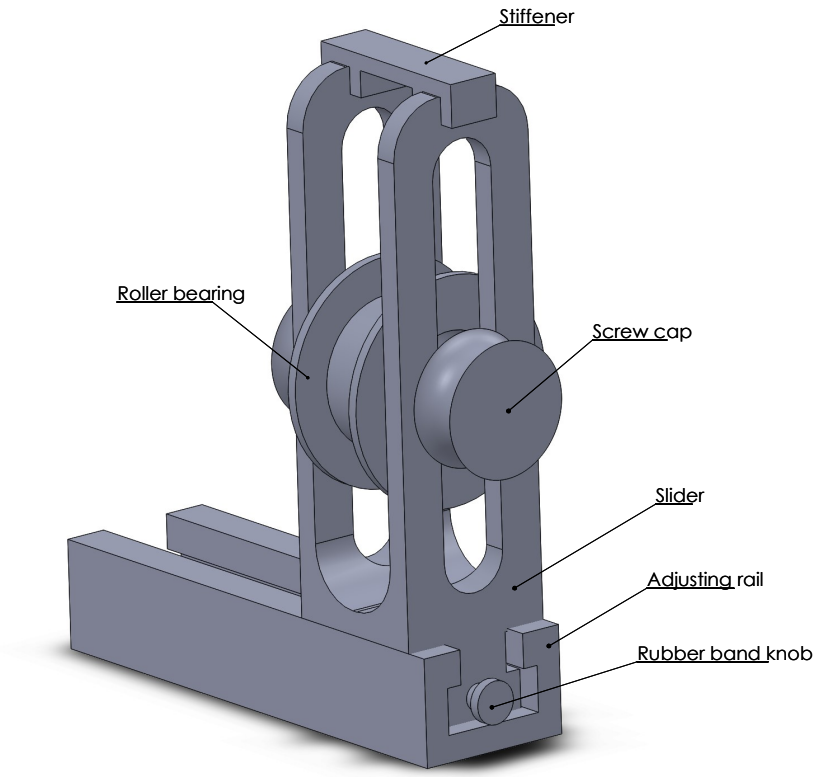

Figure 3.24: Driving the disc safely required a chain tightening mechanism for stability.

The force sensors' resistance range was measured with the help of a multimeter at 500 rpm, with an exciting current of 0 A and 4 A in each magnet. Because of heating 4 A was chosen as the absolute maximum amount of current to be run through the magnet, thereby fixing the maximum obtainable braking torque and thus the lowest force sensor resistance. A range of $160k\Omega \leq R \leq 220k\Omega$ was found and a first order RC lowpass filter was implemented by simply adding a $C = 2\,\mu$F capacitor in parallel with the 100 kΩ resistor in the force sensor circuit, as seen in Figure 3.23. The Thevenin[7] resistance range of the circuit was calculated to be:

$$61.54k\Omega = \frac{160k\Omega \times 100k\Omega}{160k\Omega + 100k\Omega} \leq R_{Th} \leq \frac{220k\Omega \times 100k\Omega}{220k\Omega + 100k\Omega} = 68.75k\Omega \tag{3.15}$$

This configuration gave a cutoff frequency (-3 dB point) range of:

$$f_c = \frac{1}{2\pi R_{Th} C} \Rightarrow 1.16Hz \leq f_c \leq 1.29Hz \tag{3.16}$$

Adding the capacitor added some slowness to the feedback loop from the measured torque, something that must be taken into consideration when designing a controller. This configuration should therefore only be used for slowly varying braking forces well below the cutoff frequency range of the filter. A capacitor charging equation for the RC filter can be given as:

$$\frac{dV_{out}}{dt} = \frac{1}{RC}\left(5V - V_{out}\right) \tag{3.17}$$

Here, V_{out} is the voltage across the capacitor thus the voltage input to the ADC. Over the braking force range the time constant[8] $\tau = R_{Th}C$ of the filter had a range of $0.12s \leq \tau \leq 0.14s$.

The chain tightening mechanism was designed in Solidworks, as seen in Figure 3.24 and 3D printed. By using rubber bands on both sides of the slider, connected to the screw cap and the rubber band knob, the roller bearing put sufficient pressure on the chain so that it became more stable. An adjusting rail was made in order to position the tightener according to the chains position. Though rather physically noisy, the solution made it possible to run the ECBT at higher speeds for longer periods of time without the risk of damage.

The sensor drift seen in Figure 3.22 became a consistent issue. The disturbance could be caused by a number of reasons, but it was narrowed down to be the PWM switching action when driving the 200 W motor, which caused problems with the ADC. Possible actions to address this problem are presented in Section 3.3.8.

[7] Thevenin's Theorem can be used to simplify circuits by e.g. replacing combinations of voltage sources and two terminal resistances with a single Thevenin voltage source and resistor. Finding the Thevenin resistance can be done by calculating the total circuit resistance after removing the load from the circuit and shorting all voltage supplies.

[8] The time constant is characterized as the time it takes for a systems' step response to reach 63.2 % of its final value.

3.3.7 Mounting a Permanent Magnet

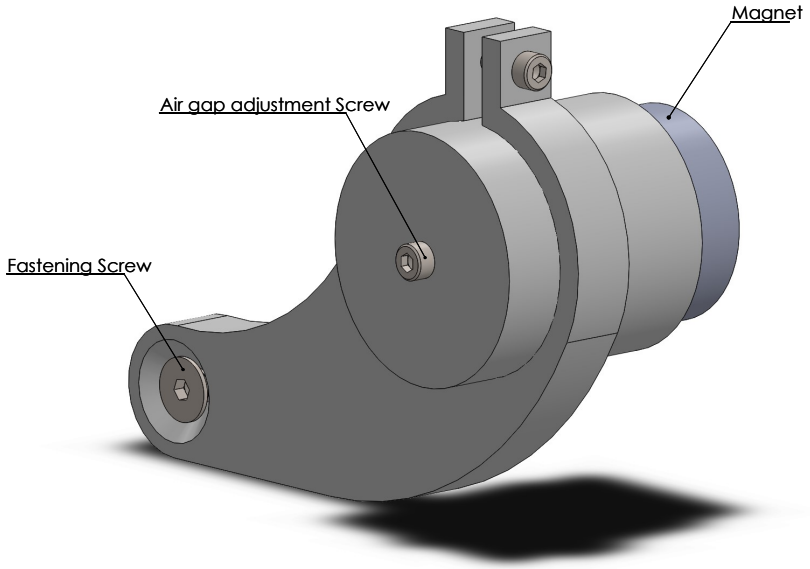

Figure 3.25: A permanent magnet mount for the ECBT, designed in Solidworks. The airgap was adjusted by twisting the indicated screw and thus sliding the magnet in and out of its sleeve.

For comparison reasons the ECBT was upgraded for testing with a neodymium magnet, which had a diameter of $D = 2.5\,\mathrm{cm}$. The field intensity at the magnets surface was measured to be $B = 0.4\,\mathrm{T}$ by using the gaussmeter. A mechanism was designed and 3D printed for fastening and for air gap adjustment, as seen in Figure 3.25. The pole center of the magnet was placed at a radius of $R = 15\,\mathrm{cm}$ from the disc axis.

3.3.8 The Resulting System

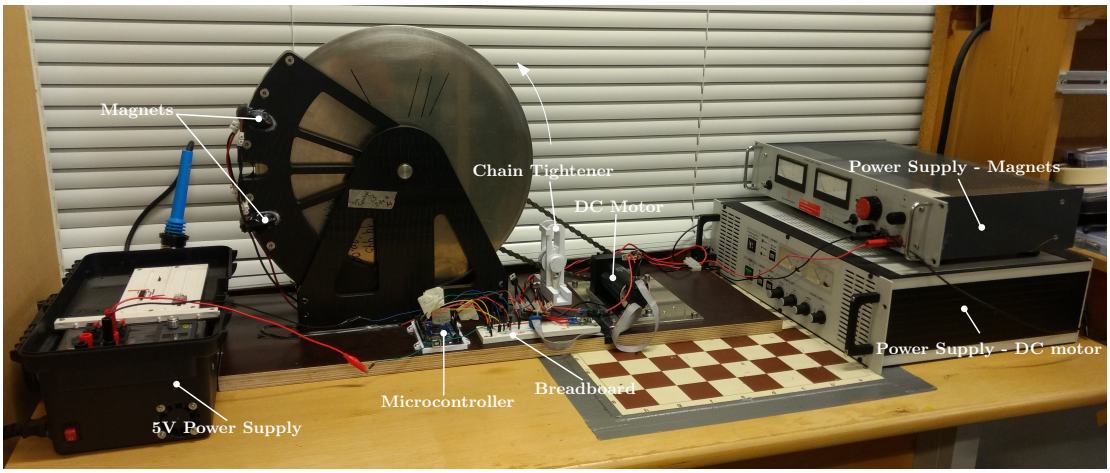

Figure 3.26: The resulting ECBT setup (permanent magnet mount not included).

Hardware design, implementation and troubleshooting in a relatively short amount of time may have affected the quality and accuracy of the system, but despite the difficulties the ECBT was implemented, calibrated and basic functionality was obtained. A picture of the resulting ECBT can be seen in Figure 3.26. Figure 3.27 shows an overview of the entire system, including the schematics. Thoughts on improvements and contributions to further work are given in Section 6.1. In the final stages of testing the magnets were unfortunately run for an excessive period of time causing the glue to soften and their position to shift, something that caused the disc to jam and the motor controller to turn up the current. The result was heating the transistor to the point that it was damaged. Luckily, data was obtained through prior testing and it was decided to spend time focusing on documentation rather than further testing and system improvements.

Overview

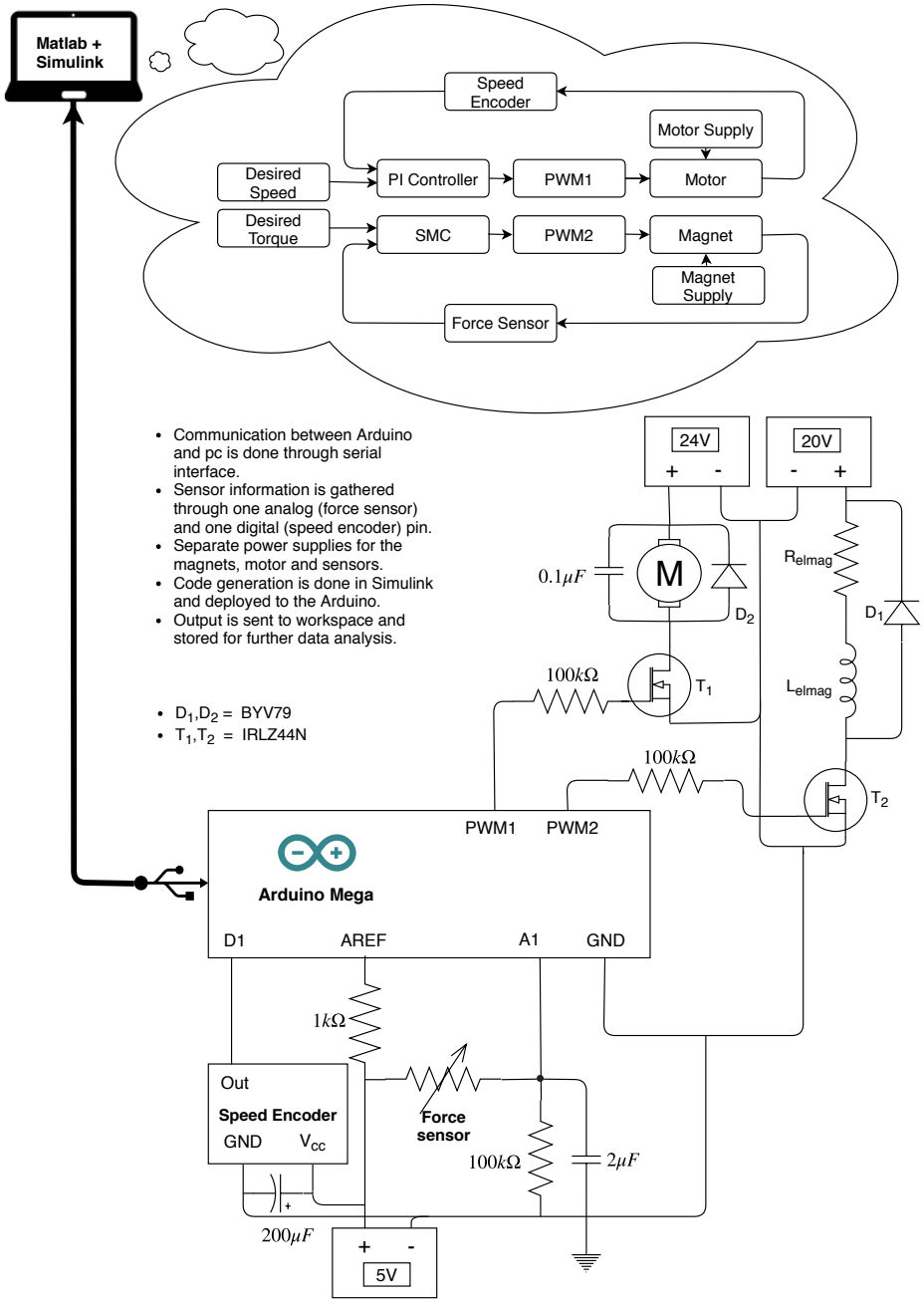

Figure 3.27: The ECBT system

Chapter 4

Real Time Torque Control

This chapter offers a brief overview of some control principles that are relevant for controlling electromagnetic brakes and thus forms a basis for torque control demonstration. Torque control on the ECBT is simulated at the end of the section. It also seeks to facilitate research by presenting some previous work done on the subject of controlling electromagnetic brakes. For linear systems there exists many well known control scheme design methods. Many systems display an approximate linear input-output relation or can be linearised about a given reference. In practice no systems are entirely without nonlinearities, and the applicability of linear control theory depends on the difference between the linearly approximated system and its real life counterpart. Large discrepancies from a linearised reference point can lead to control difficulties because the approximated model no longer matches the nonlinear system. According to Slotine et al. [32], good nonlinear control designs may be simpler than their linear counterpart, in addition to having better cost and design optimality because they are often rooted in the basic physics of the system. Tailoring linear control designs to fit highly nonlinear plants may work, but could also lead to extended development periods and therefore costs. This could also make it very difficult to use the control system on other similar applications [32]. On the other hand, nonlinear systems are mathematically complex which often makes them more difficult to describe and to obtain a good control design. The choice of an appropriate control design method therefore depends on many factors, for example; the degree of nonlinearities in the system, available development time and other resources along with the desired degree of transferability to other similar systems.

4.1 Previous Work

The literature contains several proven control methodologies for eddy current braking. Simeu and Georges [7], Anwar [16] and Lee and Park [20] are here presented, in the context of control, to aid the design of a controller capable of accurate real-time torque control of a system such as the ECBT.

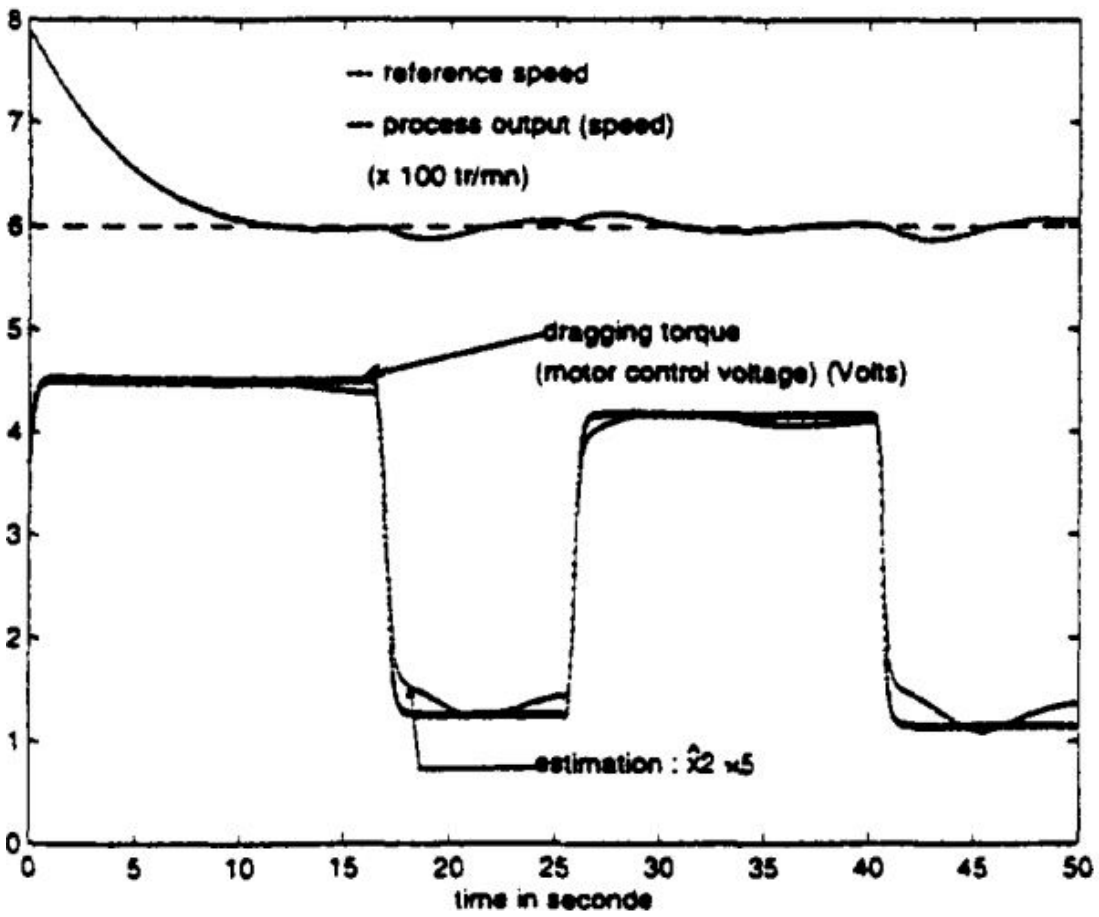

Figure 4.1: Experimental plot from Simeu and Georges [7] showing their dynamic feedback control scheme working well.

Using (2.9) Simeu and Georges [7] proposed a linearly parametrized model in which they used the rotational speed of a disc and a dragging torque applied to the process as variables. Using an input-output approach they identified the parameters of the system and created a state affine behaviour model of the system. A plot showing their experimental results is seen in Figure 4.1.

Lee and Park [20] developed an optimal torque control scheme for an eddy current brake with a rectangular footprint. This was to minimize the braking distance of an anti-lock braking system using a sliding mode controller (SMC), with the sliding surface first defined considering just the slip error, $s = e$. Steady state errors were reduced by introducing an integral term in the definition. This was based on the model in (2.14b) while compensating for leakage flux, core shape, disc heat and nonuniform flux at the edge of the pole by using the factors found in (2.8) and (2.13b). The choice of controller came from the need of compensating for varying road friction coefficients.

Anwar [15] built upon Simeu and Georges [7] by improving the accuracy of the

torque-speed characteristics. In addition, Anwar [16] patented a closed loop control algorithm for eddy current brakes. The system created an appropriate command current i_{cmd}, as referred to in Figure 3.4, from information based on rotor speed, feedback current i and desired torque. Feedback current was used to compensate for the dynamic behaviour of the current running through the retarder (i.e. inductor). To optimize the torque response, in accordance with Lee and Park [20], Anwar designed an SMC controller to compute the command current signal.

4.2 Sliding Mode Control

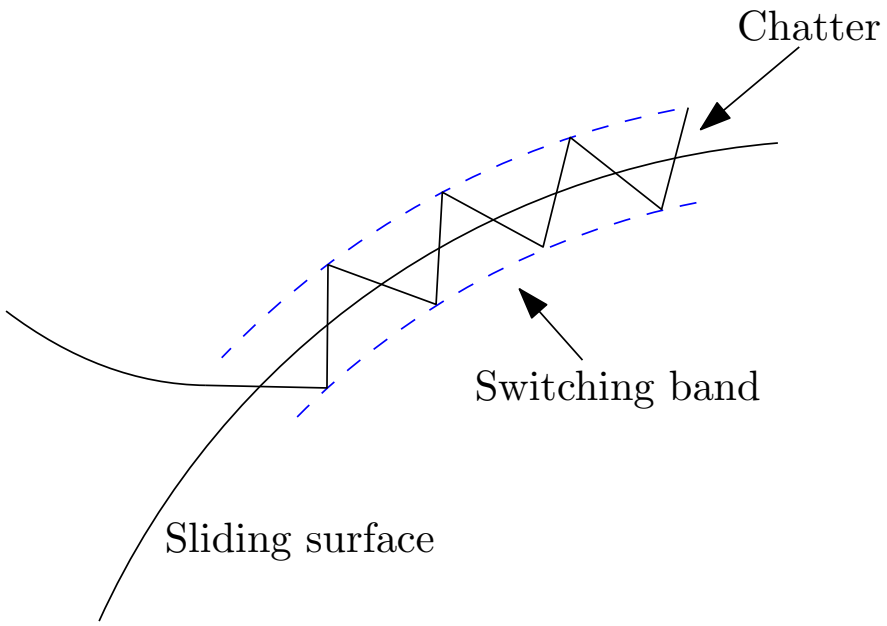

Figure 4.2: Illustration showing how the system state reaches the sliding surface and chatters across it, limited by the switching band.

The study of sliding mode controllers (SMC) started in the sixties when searching for a so-called robust control law that was insensitive to variable model parameters [33]. In its simplest form, called bang-bang control, the output switches between two discrete values. An example of this is seen in conventional electric radiators, as the output power is turned on when the room temperature goes below a certain threshold, and off when the temperature rises above it. Because of the time delay between applied heating power and the resulting change in room temperature, the temperature will oscillate about the setpoint. The time delay between the applied input and output is called hysteresis, and it is why these types of controllers also go by the name *hysteresis controllers*.

The design of a switching, or sliding mode controller can be split into two parts:

- Sliding surface design that drives the error to zero when the dynamical behaviour is confined to it.
- Design of a feedback controller gain that drives the system towards and keeps it on the sliding surface.

The first and the most challenging task is to find a function of the error that converges to zero when on the sliding surface, i.e. $s = 0$, and there are numerous ways of defining it. Secondly, a feedback controller must be designed to drive the system towards the sliding surface and keep it there. Stability can be proved by

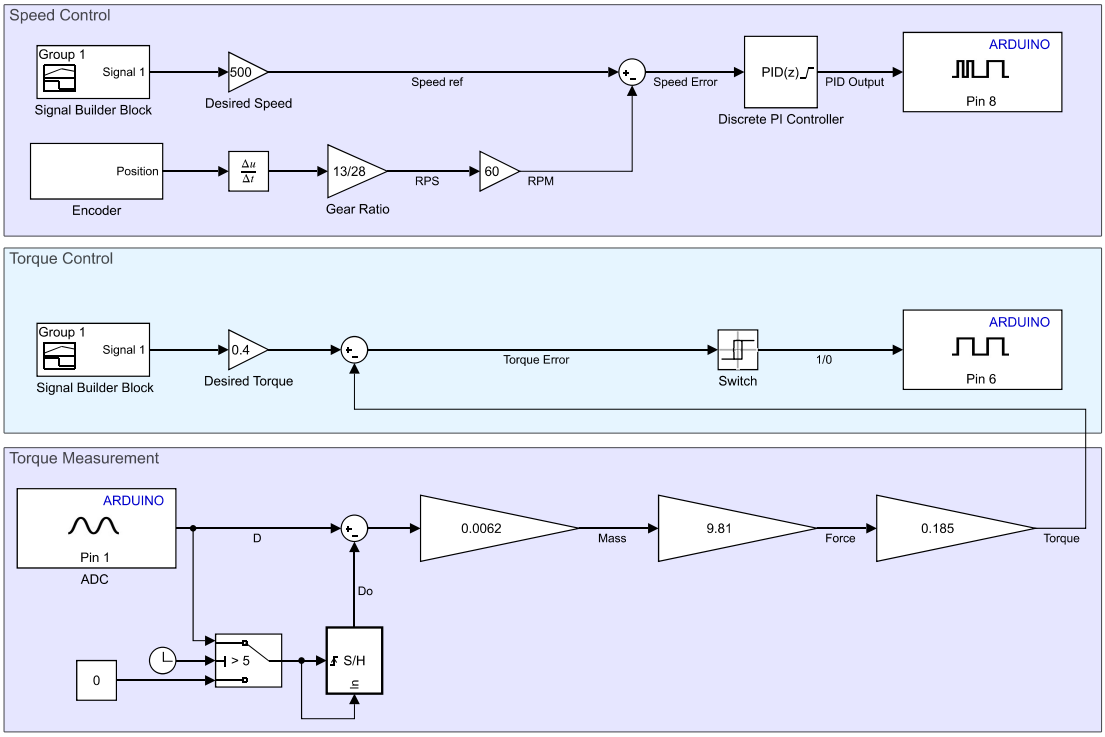

Figure 4.3: Simulink diagram showing the ECBT torque control system.

using Lyapunov theory. By choosing an appropriate Lyapunov function candidate of the sliding surface, often given by $V(s) = \frac{1}{2}s^2$, stability can be demonstrated by proving that the controller output $u(t)$ drives the deviations from the sliding surface to zero in finite time [34].

For first order sliding mode control the input can be given as:

$$u(t) = -Usign(s) \Leftrightarrow u(t) = \begin{cases} -U & \text{for } s > 0 \\ U & \text{for } s < 0 \end{cases} \tag{4.1}$$

Here, U is a constant gain that is set in accordance to the specifics of the system. In the example of heating of a room, U could correspond to the power output of a radiator. A negative control output $-U$ could correspond to a cooling element of equal power. This is why first order sliding mode is also referred to as switching mode control, because it switches between two discrete values of output. A threshold about the sliding surface is defined by the switching band, as illustrated in Figure 4.2. The figure also shows something called chattering, a phenomena that can be undesired in some types of systems, specifically ones where mechanical wear could be an issue. Chattering can be addressed by replacing the discontinuous controller output with a continuous smooth approximation. Several other

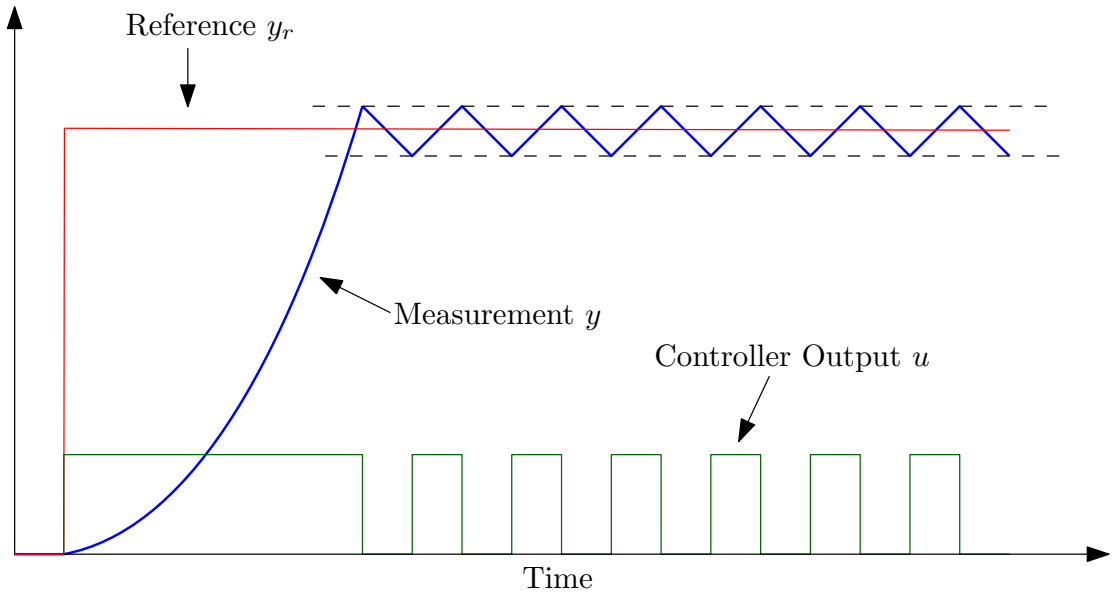

Figure 4.4: Visualization of an on/off control system behaviour.

variations of sliding mode control also exists that are not presented here. These could be investigated during further research on the ECBT.

To demonstrate real-time torque control a bang-bang controller was implemented in this thesis because of its documented use and feasibility which, as mentioned, is the simplest form of a sliding mode controller. The sliding surface s of a bang-bang controller is the error e:

$$s = e = y - y_r \tag{4.2}$$

Here, in the case of the ECBT, y_r is the desired braking torque and y is the measured torque. The controller outputted a binary signal that was used to open and close the electric circuit supplying the magnets with current:

$$u(t) = H(s) = \begin{cases} 0 & \text{for } s > 0 \\ 1 & \text{for } s < 0 \end{cases} \tag{4.3}$$

The voltage was set to a constant value and the on and off thresholds of the relay was set to 0.02 Nm and -0.02 Nm, respectively. The bang-bang controller proved to be a suitable way of testing basic control considering the hardware design of the system. By connecting the controller output to an Arduino digital-output-block as seen in Figure 4.3, the magnets MOSFET-switch could be switched on and off, effectively working as a relay producing a pulse-width modulated signal that controlled the current and hence the braking torque. See figure 4.3 for an overview of the ECBT torque control system.

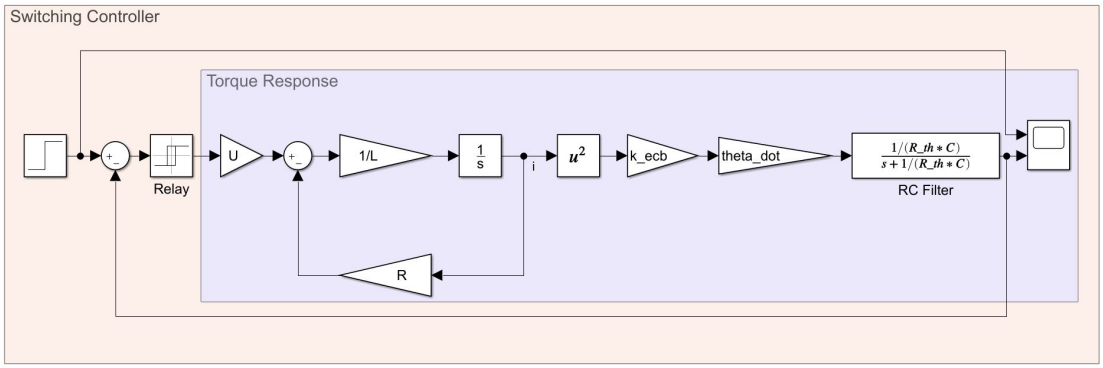

Figure 4.5: The Simulink block diagram used for simulating the torque response of the ECBT using an SMC, including the effect of the delay resulting from the RC filter as explained in Section 3.3.6. The braking constant k_{ecb} was calculated using (2.14b) from the parameters given in Table 3.1, while using the compensatory factors c and α.

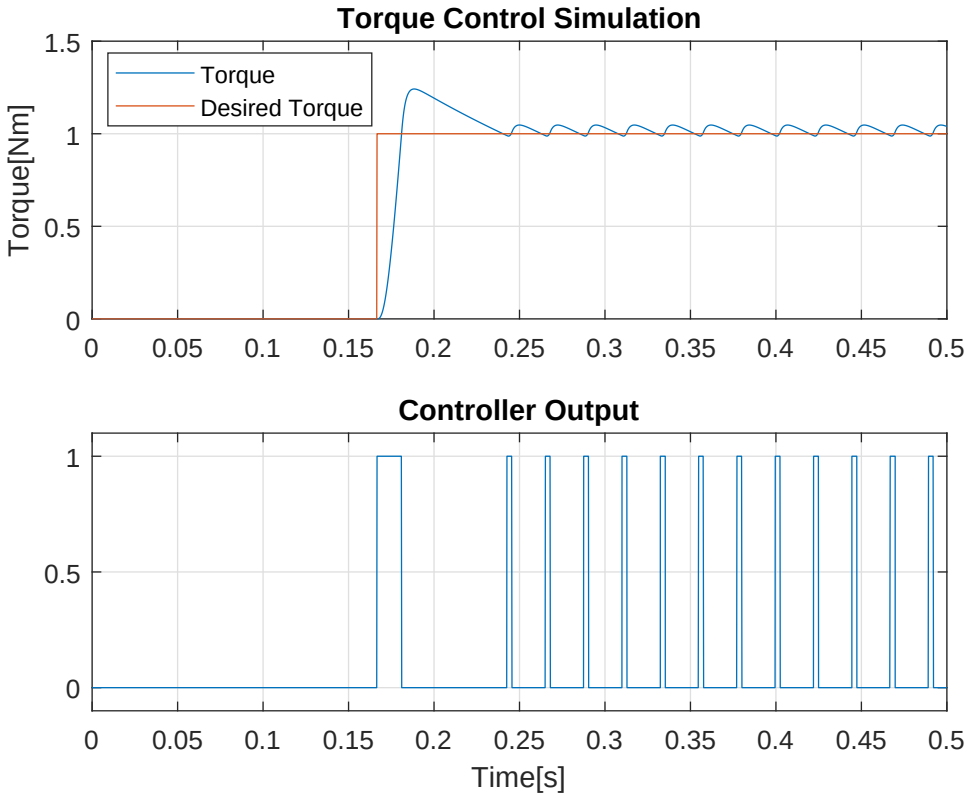

Figure 4.6: Simulated torque response with the switching controller.

Writing the command current to the electromagnets as $i_{cmd} = U/R_{mag}$, (3.4) can be written as:

$$\frac{di}{dt} = \frac{1}{L}(U - R_{mag})i \tag{4.4}$$

Here, L is the combined inductance of the parallel magnets, U is the applied volt-

age and R_{mag} is the total electrical resistance of the magnets.

Equation (4.4) was implemented in a Simulink diagram as shown in Figure 4.5, to simulate the currents' response. The inductance of the magnets was measured to be $L = 5.92\,\text{mH}$ by the use of an LCR meter and the total resistance was measured to be R_{mag} =2.1 Ω. Using (2.14b), (3.3) and the compensatory factor c and α, the braking torque τ_b can be given as:

$$\begin{aligned}\tau_b &= \frac{n\pi\sigma}{4} D^2 d \left(\frac{\mu_0 N}{2l_g + d}\right)^2 R^2 c\alpha\dot{\theta} i^2 \\ &= k_{ecb}\dot{\theta} i^2\end{aligned} \tag{4.5}$$

The model parameters from Table 3.1 was used together with the measured quantities R_{mag} and L to simulate the system. The voltage across the magnets was set to $U = 20\,\text{V}$. Effects of time delay resulting from the RC filter was accounted for by implementing a transfer function block of such a filter with the given parameters:

$$T(s) = \frac{\frac{1}{R_{Th}C}}{s + \frac{1}{R_{Th}C}} \tag{4.6}$$

As explained in Section 3.3.6, R_{Th} and C is the Thevenin resistance of the RC filter and C is the capacitance. The simulation seen in Figure 4.6 shows an overshoot before reaching and oscillating across the sliding surface $s = e$, in addition to a relatively small steady state error. The results were considered satisfactory in order to proceed with experimental testing and torque control demonstration.

Chapter 5

Experimentation and Results

As noted in Section 3.3.6, the force measurements were subject to disturbances most likely coming from the PWM signal controlling the motor in addition to mechanical noise and sensor issues. Because the magnets were measured to be of equal electric resistance at room temperature, they were assumed to be so throughout the experiment and therefore conducting an equal amount of current. Differences in temperature may have caused deviations from this assumption. The compensation factors c and α, as explained in Section 2.3, were taken into account when comparing experimental data with the theoretical torque but even larger deviations were seen. These discrepancies could be explained not only from the inaccuracies in the system itself, i.e disturbances and/or an unreliable ADC, but also from the assumptions that the theory is based on (infinite sheet, no fringing etc.). This chapter presents the data and discusses the findings gathered during this project.

5.1 Torque vs Speed

5.1.1 Electromagnets

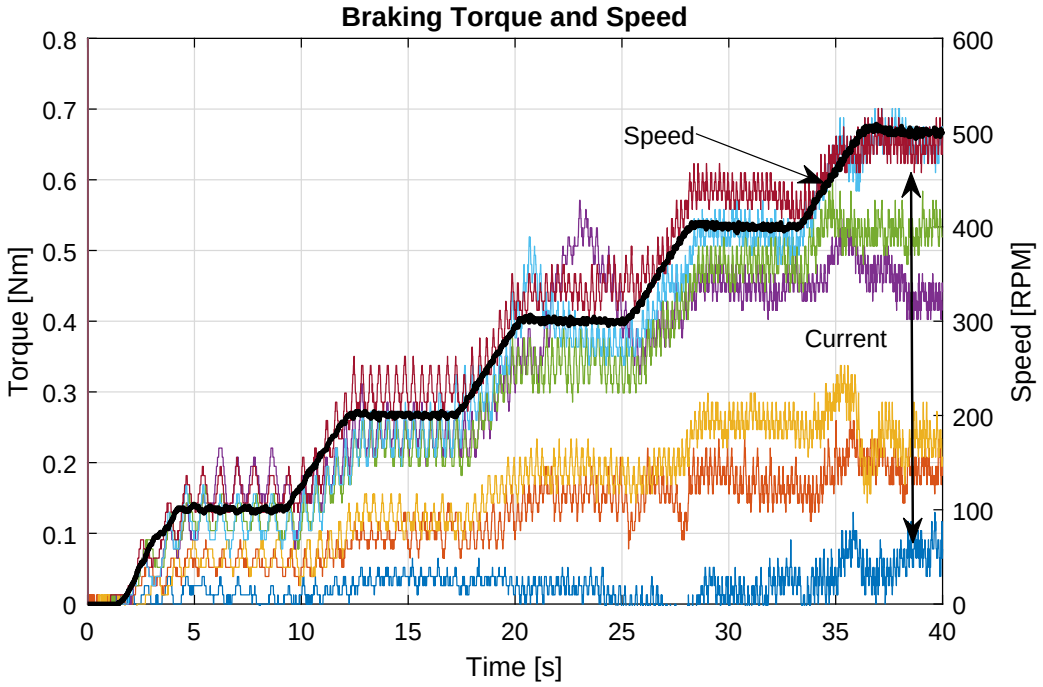

Figure 5.1: Raw data of a speed staircase with five second plateaus at 100-500 rpm, with input currents ranging from 1-4 A with steps of 0.5 A.

Due to the limitations of the ECBT's mechanical construction it was tested at speeds up to 500 rpm. Higher speeds tended to induce vibrations large enough to make the pole faces touch the disc and the chain movement caused the sprockets failing to grasp the chain properly. To get a better approximation of torque at different speeds, because of the known disturbances, the motor was driven in a staircase manner at plateaus between 100-500 rpm as seen in Figure 5.1 at currents ranging from 1-4 A, which corresponded to a field intensity in the magnets of 0.11-0.40 T and 0.15-0.57 T, respectively. Figure 5.1 shows the noise to be more disturbing to the measurements at lower levels of field intensity, something that is likely because of a high noise-torque ratio lowering the resolution of the measurement. Amplitude and frequency of the noise was not measured and it is something that could be investigated during further troubleshooting the ECBT. Though noise is apparent, Figure 5.1 shows that the torque clearly increases with field intensity and speed. The relationship between torque and speed shows a proportional nature within the range of testing, but these measurements do not clearly bring forth the quadratic effect of increasing field intensity, as it in theory should.

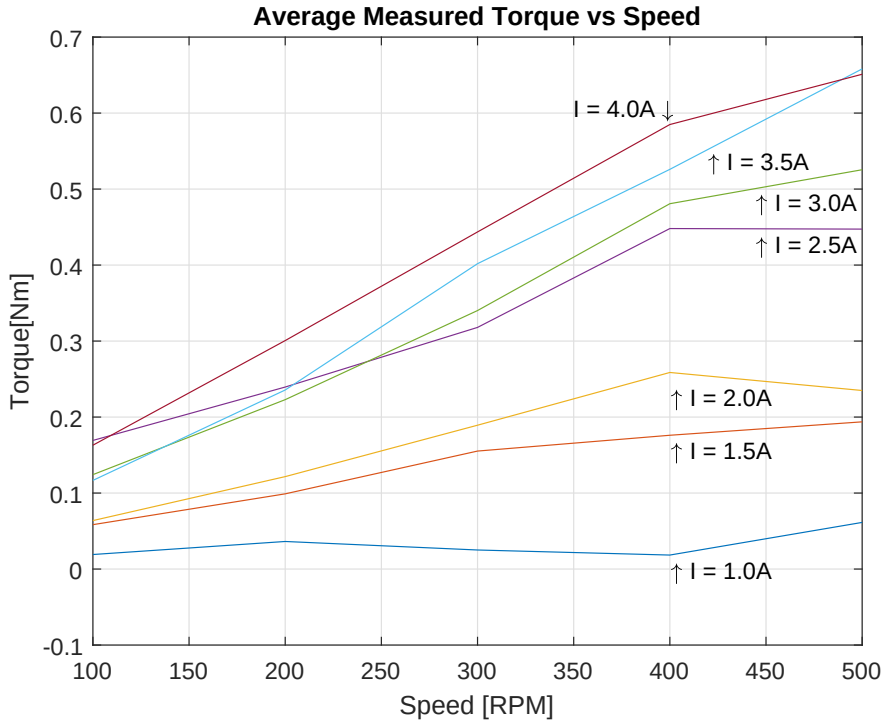

Figure 5.2: The average values of torque at each speed plateau show a more clear picture of the braking force compared to speed and exciting current.

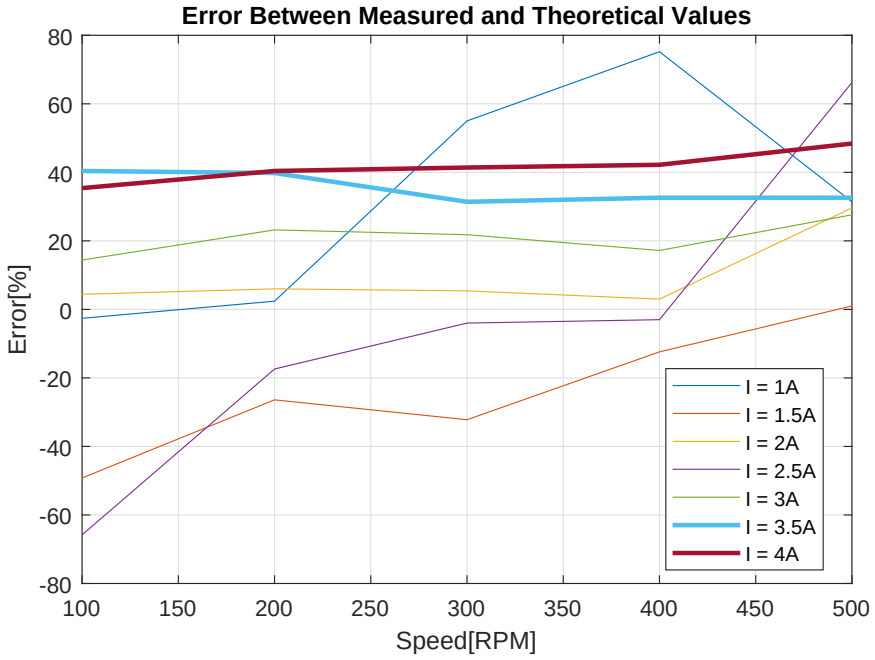

Figure 5.3: The error seems to be more stable at higher exciting currents, at about 40%, as the thicker lines indicate.

Speed [RPM]	Current [A]	Measured Torque [Nm]	Theoretical Torque [Nm]	Ratio
100	1	0,019	0,019	1,026
	1,5	0,058	0,039	1,493
	2	0,064	0,067	0,956
	2,5	0,169	0,102	1,659
	3	0,124	0,145	0,857
	3,5	0,117	0,195	0,597
	4	0,163	0,253	0,645
200	1	0,036	0,037	0,976
	1,5	0,099	0,078	1,264
	2	0,125	0,133	0,940
	2,5	0,239	0,204	1,174
	3	0,223	0,290	0,768
	3,5	0,236	0,391	0,603
	4	0,301	0,505	0,595
300	1	0,025	0,056	0,451
	1,5	0,155	0,117	1,323
	2	0,189	0,200	0,945
	2,5	0,318	0,306	1,039
	3	0,340	0,435	0,782
	3,5	0,402	0,586	0,686
	4	0,444	0,758	0,586
400	1	0,018	0,074	0,248
	1,5	0,176	0,157	1,125
	2	0,259	0,267	0,969
	2,5	0,448	0,435	1,029
	3	0,481	0,580	0,828
	3,5	0,526	0,782	0,673
	4	0,585	1,010	0,579
500	1	0,064	0,093	0,686
	1,5	0,194	0,196	0,990
	2	0,235	0,334	0,704
	2,5	0,173	0,510	0,339
	3	0,526	0,726	0,724
	3,5	0,658	0,977	0,674
	4	0,651	1,263	0,516

Table 5.1: This table compares the measured data with the theoretical model in equation 2.14b, multiplied by the factor c and α to compensate for the finite disc and fringing effects, respectively.

At each plateau the average value of the measurement was taken to give a better approximation of the torque at the given speed. The plot in Figure 5.2 shows the results and the linearity between torque and speed is apparent.

As seen in both Figure 5.1 and 5.2 the current ECBT is not suited for measurement of lower levels of torque due to the disturbances, higher field levels tended to give more stable and repeatable results. Section 5.1.1 shows a table comparing the measured and the theoretical torque values at each speed and current levels. The theoretical values was compensated with the factor α to take fringing effects into account, and computed using the measured field intensity at the respective current levels. As highlighted in green, the top levels of applied field intensity gave the most repeatable errors, being roughly 60% of the theoretical estimate. The errors between the theoretical values at each exciting current and speed indicate that the ECBT gives more reliable readings at higher field intensities and therefore torque, because of the fact that more stable errors were seen. Figure 5.3 shows the torque level error up to 3.5 A to fluctuate greatly, and the data may indicate that an additional compensation factor of 0.6 is suitable for the current ECBT, but this hypothesis should be tested further by using other configurations of pole diameters, air gaps and current levels.

5.1.2 Permanent Magnet

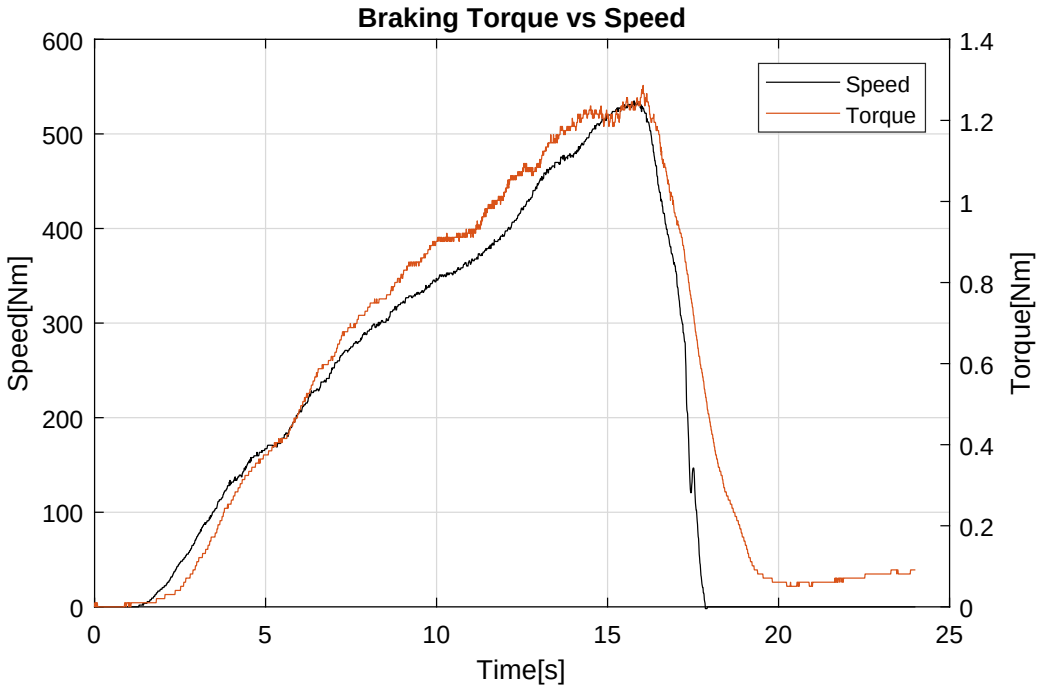

Figure 5.4: Raw data of measuring torque when using a permanent magnet and measuring 0.4 T on the disc surface, under the pole projection area, and controlling the motor without PWM.

Testing with the permanent magnet was done manually by adjusting the motor current on the power supply, with the aim of eliminating PWM interferences with the readings. The speed was adjusted up to just above 500 rpm while torque measurements were collected with Simulink. The air gap was adjusted and the magnetic field was measured using the gaussmeter at the surface of the disc, right under the center of the pole projection area. Figure 5.4 displays the raw data of the readings and shows that the noise is almost eliminated. It also shows roughly a doubling in braking torque, which can be explained by the much larger pole diameter.

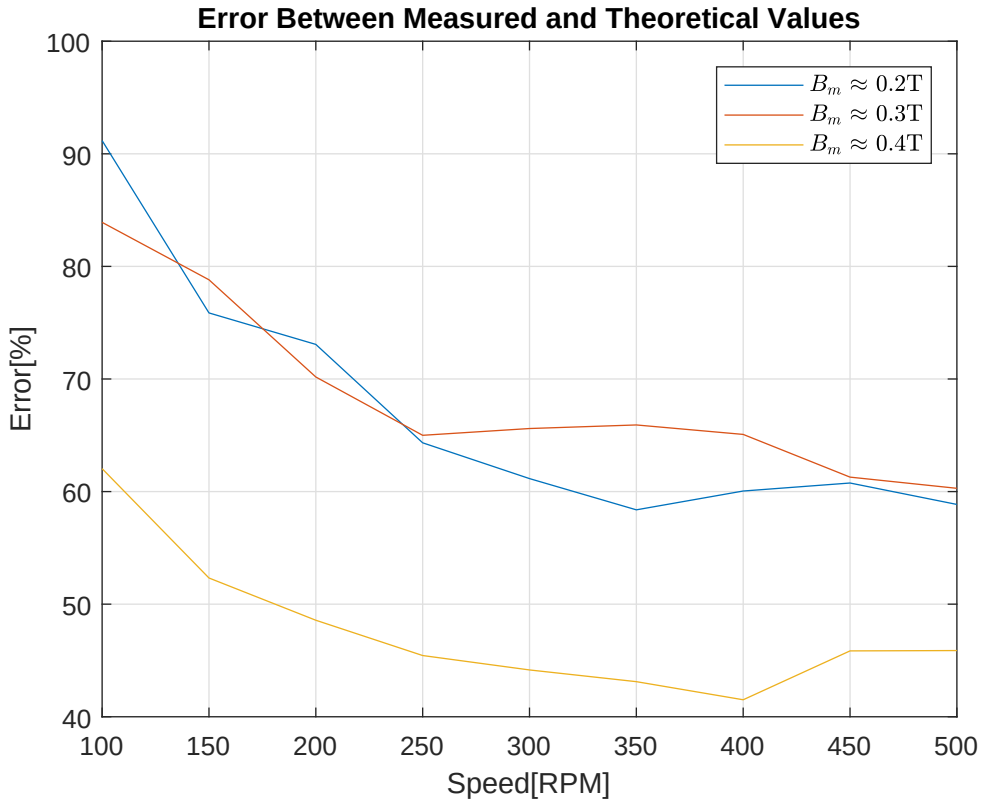

Figure 5.5: The data collected from the permanent magnet also show the error to converge as the speed, and thus torque, increases.

The error plot in Figure 5.5 shows more error than with the electromagnets, something that could be explained by a larger fringing effect as the air gap was up to 1cm. The configuration, a single magnet on one side of the disc, also most likely increased this effect. Nonetheless, the data shows the error converging with increased speed and thus higher torque. This strengthens the idea that the measurement is more accurate at higher torque levels.

5.2 Demonstrating Torque Control

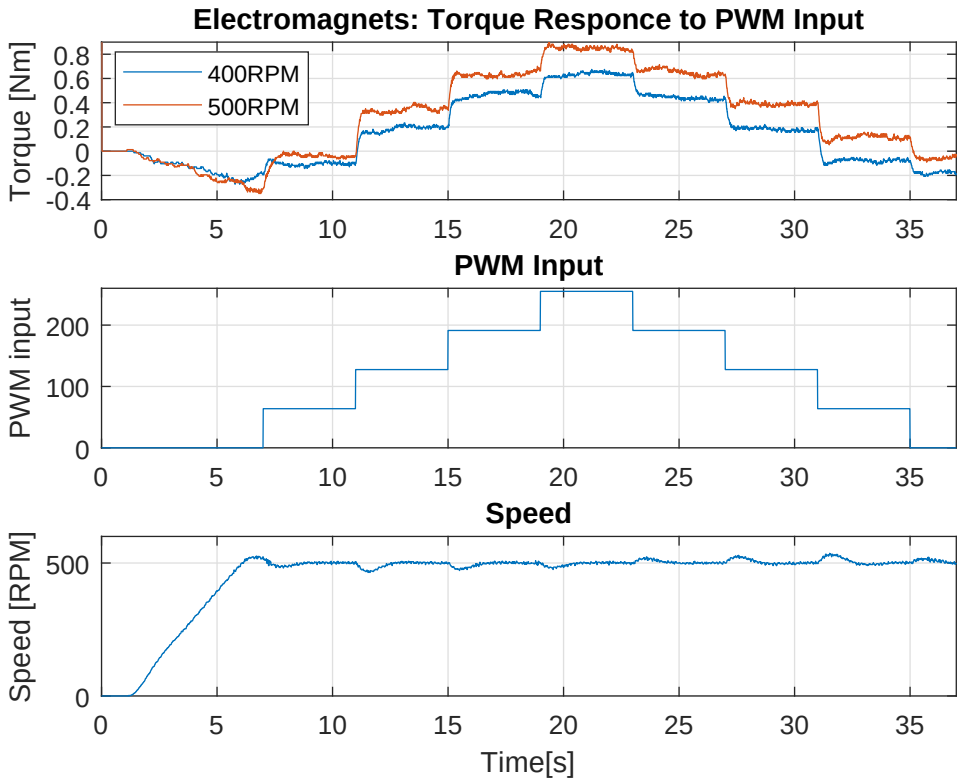

Figure 5.6: Testing torque control with a pulse-width modulated signal input.

At 400 and 500 rpm the ECBT was tested by controlling the current with a PWM staircase input, an input of 255 meaning 100% duty cycle. The voltage across the magnets was set to be a constant 20 V, meaning that the current through each magnet at full duty cycle was:

$$I_{magnet} = \frac{1}{2} \cdot \frac{20V}{\frac{4.2\Omega}{2}} = 4.76A \tag{5.1}$$

These high current levels gave better measurements, though one can see considerable sensor drift in the beginning when accelerating the disc. Heating of the magnets should also have affected the resistance of the magnets, effectively reducing the current running through them. For example, heating the entire magnet from room temperature 20 °C to 60 °C, gives a resistance of:

$$R = R_0 \left[1 + \alpha \left(T - T_0\right)\right] = 4.2\Omega \left[1 + \frac{3.9 \cdot 10^{-3}}{^\circ C} \left(60^\circ C - 20^\circ C\right)\right] = 4.9\Omega \tag{5.2}$$

Which gives a current of 4.12 A when using a voltage of 20 V. Having a constant voltage source the current should theoretically have decreased somewhat from

I[A]	B[mT]	Error[%]
0,0	14,3	
0,5	63,5	
1,0	119,5	
1,5	166,4	
2,0	216	
1,5	184	+9,57
1,0	130,8	+8,64
0,5	74,4	+14,65
0,0	14,77	+3,18

Table 5.2: The data shows remanent magnetization in the core when decreasing the current.

the first plateau on the left side of the staircase to the equivalent plateau on the right side. In fact, Figure 5.6 shows the torque at 500 rpm to actually *increase* significantly from the plateau at 7-11 s to the one at 31-35 s, while being more consistent at higher torque. Some testing of the magnets themselves revealed the reason for this to be magnetic remanence. Post testing with the ECBT, one of the magnets were tested with the gaussmeter. While having the probe at exactly the same location in the airgap the field was measured while ramping up the current from zero to 2 A and back. The results from this test, seen in Table 5.2, indicate that the higher torque at the descent part of the staircase is caused by remanence in the magnets themselves. This is something that must be considered for more accurate control schemes.

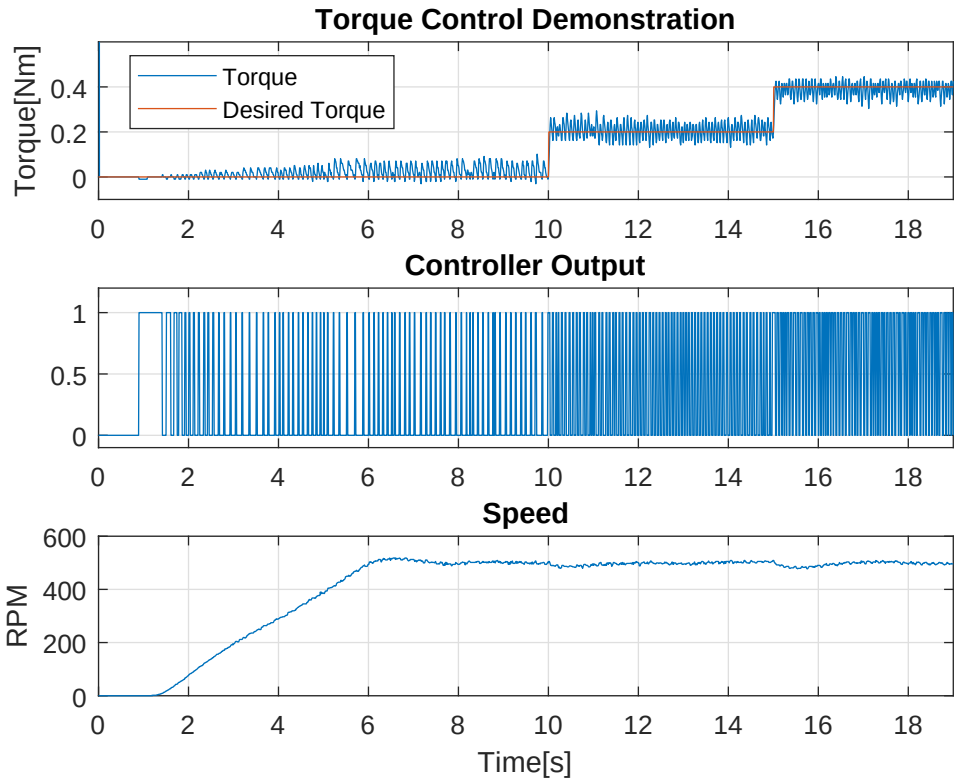

Figure 5.7: Real-time torque control demonstration.

For torque control, as explained in Section 4.2, the ECBT was tested with a sliding mode/switching controller. Hysteresis was set to $\pm 0.02\,\text{Nm}$ and the reference was designed as a step response from 0-0.2 and 0.2-0.4 Nm respectively. The system response is seen in Figure 5.7 and it shows successful demonstration of torque control, with the expected chattering phenomena that occurs as a result of the switch turning on and off. The chatter is most likely amplified by the PWM noise coming from the motor controls. The controller output starts switching the same moment the motor starts accelerating, which highlights the fact that it is trying to compensate for the resulting sensor drift.

5.3 Summary

The experimental study done in this thesis displayed the following:

- Rotational speed and braking torque show a proportional relationship.
- Magnetic field strength and braking torque do *not* seem to show a quadratic relationship.
- Fringing effects and non-uniform magnetic field density in the air gap can have great influence on eddy current density in the pole projection area, more than the compensatory factor α can account for, thus reducing the braking force. This reduces the viability of model (2.14b) used for theoretical comparison.
- The ECBT shows more reliable readings at higher torque levels, and the results hint that an additional compensatory factor of 0.6 should be used for a configuration with the parameters given in Table 3.1.
- The torque behaviour observed when using a single permanent magnet hint that the compensatory factor should be adjusted to fit each independent configuration.
- Disturbances from high current switching is evident, something that reduces the resolution of the measurements.
- Real-time torque control is indeed possible with a simple switching controller.

Chapter 6

Conclusion

This thesis has resulted in a first prototype of an eddy current braking testbed. The prototype was successfully designed and implemented and was proven feasible through experimental testing, though there are several areas of potential improvement. Large deviations from theory with regards to both expected torque and electromagnet dimensioning were seen and discussed, and recommendations for further work are given in this chapter. It is thought that fringing due to a large airgap and an uneven winding technique caused the magnetic flux lines to deviate from the pole projection area to a degree to which the validity of the theoretical models was reduced, and beyond the degree of what the factor α could compensate for. Variations in the conductivity of the disc could also have affected the torque level. Measurements at the higher torque levels hint that an additional compensation factor of 0.6 could be suitable for this system when using this specific configuration, though this hypothesis should be further investigated. Magnetic remanence was documented and could have affected the accuracy of the theoretical comparison. Torque control was successfully demonstrated with a sliding mode controller at the end of the project. Many factors influencing both the practicalities of eddy current brakes along with the interaction of all the physical elements and phenomena in such a system was highlighted in this thesis. The goal of facilitating further research on eddy current brakes is therefore regarded as achieved.

6.1 Further Work

6.1.1 Force Sensor Issues

If direct force measurement is to be utilized, more research on force sensors should be done for this type of application, this being one of the largest sources of error in the system as it is. Specifically, piezoresistive resistors may not be the best choice in this case because of drifting and hysteresis issues. Hollinger and Wanderley [31] compared the Tekscan with two other sensors and showed that it had the most consistent drift, but had more noise and a considerably larger drift time. When applying repeated force peaks two minutes apart, as seen in Figure 6.1, they

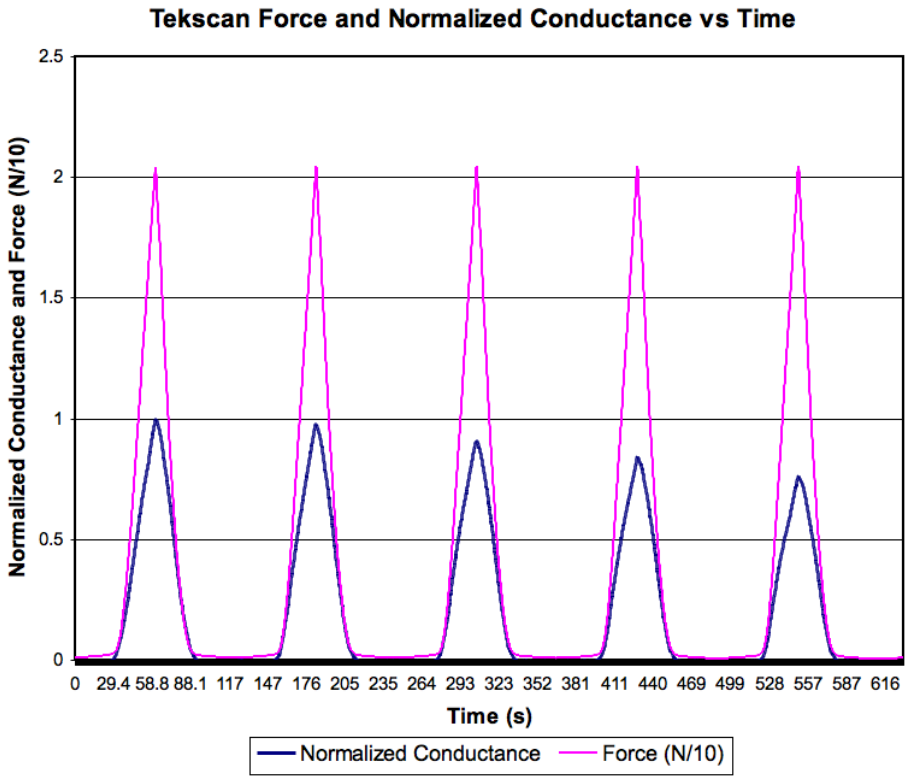

Figure 6.1: Hollinger and Wanderley [31] showed the conductivity of the Tekscan to decrease with each applied force peak.

showed that the Tekscan had a decrease in conductivity at each peak, and after five peaks it was down to 75% of the first. This brings up the fact that this kind of sensor is not suited for an application with varying forces of relatively high frequency as in the ECBT, compared to more static systems. It also explains why the zero-mass-output increases after each force peak in the measurements taken during calibration, seen in Figure 3.21, Section 3.3.5. Another method of sensing braking torque is by measuring the supply current to the motor. With the controller running the motor at a constant speed the current has to be increased upon braking in order to stabilize the system about the reference. The difference in the motors power output is an indirect measurement of the ECBs braking power. For further research on the ECBT, this is a recommended sensing method.

6.1.2 Mechanical Construction

It is proposed that a fixed gear solution with a ratio of at least 13/28 would be a better power transmission option, with a more robust tightening mechanism and possibly a belt drive for smoother motion or connecting a more powerful motor directly to the shaft. The disc and shaft should be crafted to a better accuracy in order to achieve a more stable mechanical setup, and it should be stiffened more.

6.1.3 Magnets

Considering the consistent differences between theory and practice when it comes to the measured field intensity in the air gap of each magnet, the length of the magnetic core should be made considerably longer in order to minimize the cross sectional difference between the core and the outer windings. Winding should be done evenly to minimize fringing effects. A new, more heat resistant fastening mechanism must be designed to be able to run larger amounts of current through the magnets for longer periods of time without them loosening. A cooling fan would also be beneficial, and the distance between the pole surface and disc should be increased somewhat to reduce the risk of the magnet touching the disc surface when spinning.

6.1.4 Wiring Layout and Transistors

The wiring of the system should be made more tidy and moved from a prototyping breadboard to a more reliable circuit board. Care should be taken in order to make sure the ground connections are star connected and not daisy chained, especially considering the large currents drawn from the magnets and motor. Wires from the PWM output of the microcontroller should be separated as much as possible from the force sensor wiring to reduce risk of noise. Bypass capacitors must be placed between terminals from all power supplies, as close to the circuit as possible, to reduce voltage spikes from the PWM switching action. Hopefully these measures will reduce the risk of disturbances affecting the sensor outputs. Transistors should be fitted with suitable heat sinks to be more robust in an over-current-event.

Bibliography

[1] W. Smythe, "On eddy currents in a rotating disk," *Electrical Engineering*, vol. 61, no. 9, pp. 681–684, 1942.

[2] D. Schieber, "Braking torque on rotating sheet in stationary magnetic field," in *Proceedings of the Institution of Electrical Engineers*, vol. 121, no. 2. IET, 1974, pp. 117–122.

[3] H. Wiederick, N. Gauthier, D. Campbell, and P. Rochon, "Magnetic braking: Simple theory and experiment," *American Journal of Physics*, vol. 55, no. 6, pp. 500–503, 1987.

[4] M. A. Heald, "Magnetic braking: Improved theory," *American journal of physics*, vol. 56, no. 6, pp. 521–522, 1988.

[5] J. Wouterse, "Critical torque and speed of eddy current brake with widely separated soft iron poles," in *IEE Proceedings B (Electric Power Applications)*, vol. 138, no. 4. IET, 1991, pp. 153–158.

[6] P. Yannopoulos-Lascaratos and J. Tegopoulos, "Eddy-current distribution in cylindrical structures caused by rotating magnetic fields," in *IEE Proceedings B (Electric Power Applications)*, vol. 129, no. 2. IET, 1982, pp. 64–74.

[7] E. Simeu and D. Georges, "Modeling and control of an eddy current brake," *Control Engineering Practice*, vol. 4, no. 1, pp. 19–26, 1996.

[8] L. Barnes, J. Hardin, C. A. Gross, and D. Wasson, "An eddy current braking system," in *System Theory, 1993. Proceedings SSST'93., Twenty-Fifth Southeastern Symposium on.* IEEE, 1993, pp. 58–62.

[9] W. Peterson, "Numerical solution of eddy current problems in ferromagnetic bodies travelling in a transverse magnetic field," *International journal for numerical methods in engineering*, vol. 58, no. 12, pp. 1749–1764, 2003.

[10] N. Burais, A. Foggia, A. Nicolas, J. Pascal, and J. Sabonnadiere, "Numerical solution of eddy currents problems including moving conducting parts," *IEEE Transactions on magnetics*, vol. 20, no. 5, pp. 1995–1997, 1984.

[11] Conraths, "Eddy current and temperature simulation in thin moving metal strips," *International journal for numerical methods in engineering*, vol. 39, no. 1, pp. 141–163, 1996.

[12] K. Karakoc, E. J. Park, and A. Suleman, "Improved braking torque generation capacity of an eddy current brake with time varying magnetic fields: A numerical study," *Finite elements in Analysis and Design*, vol. 59, pp. 66–75, 2012.

[13] K. Lee, K. Park, J. Kang, and S. Wang, "Torque analysis and optimization of an eddy current brake system," *Proc. of IMCSD*, vol. 99, pp. 137–141, 1999.

[14] C. W. T. McLyman, *Transformer and inductor design handbook*. CRC press, 2016.

[15] S. Anwar, "A parametric model of an eddy current electric machine for automotive braking applications," *IEEE transactions on control systems technology*, vol. 12, no. 3, pp. 422–427, 2004.

[16] ——, "Closed-loop control algorithm for an eddy current braking system," Sep. 16 2003, uS Patent 6,619,760.

[17] A. H. Gosline and V. Hayward, "Eddy current brakes for haptic interfaces: Design, identification, and control," *IEEE/ASME Transactions On Mechatronics*, vol. 13, no. 6, pp. 669–677, 2008.

[18] A. Association *et al.*, *Aluminum: properties and physical metallurgy*. ASM International, 1984.

[19] A. Lucía, J. Hoyos, and J. L. Chicharro, "Preferred pedalling cadence in professional cycling," *Medicine & Science in Sports & Exercise*, vol. 33, no. 8, pp. 1361–1366, 2001.

[20] K. Lee and K. Park, "Optimal robust control of a contactless brake system using an eddy current," *Mechatronics*, vol. 9, no. 6, pp. 615–631, 1999.

[21] G. Sokolov *et al.*, "Analysis of electrodynamic brake for utilization in systems with rotating shafts," 2016.

[22] H. Danan, A. Herr, and A. Meyer, "New determinations of the saturation magnetization of nickel and iron," *Journal of Applied Physics*, vol. 39, no. 2, pp. 669–670, 1968.

[23] A. D'Ausilio, "Arduino: A low-cost multipurpose lab equipment," *Behavior research methods*, vol. 44, no. 2, pp. 305–313, 2012.

[24] R. Barber, M. Horra, and J. Crespo, "Control practices using simulink with arduino as low cost hardware," *IFAC Proceedings Volumes*, vol. 46, no. 17, pp. 250–255, 2013.

[25] Maxon, "Re50200w." [Online]. Available: https://www.maxonmotor.com/medias/sys_master/root/8797181181982/RE-50-50-GB-200W-2WE-mTerminal-Detail.jpg

[26] MathWorks, "What is an s-function?" [Online]. Available: https://se.mathworks.com/help/simulink/sfg/what-is-an-s-function.html

[27] ——, "Device driver blocks." [Online]. Available: https://se.mathworks.com/help/supportpkg/raspberrypi/device-driver-blocks.html

[28] ——, "Device drivers." [Online]. Available: https://se.mathworks.com/matlabcentral/fileexchange/39354-device-drivers

[29] Arduino.cc, "analogread()." [Online]. Available: https://www.arduino.cc/reference/en/language/functions/analog-io/analogread/

[30] ——, "analogreference()." [Online]. Available: https://www.arduino.cc/reference/en/language/functions/analog-io/analogreference/

[31] A. Hollinger and M. M. Wanderley, "Evaluation of commercial force-sensing resistors," in *Proceedings of the International Conference on New Interfaces for Musical Expression, Paris, France*, 2006, pp. 4–8.

[32] J.-J. E. Slotine, W. Li *et al.*, *Applied nonlinear control*. Prentice hall Englewood Cliffs, NJ, 1991, vol. 199, no. 1.

[33] W. Perruquetti and J.-P. Barbot, *Sliding mode control in engineering*. CRC Press, 2002.

[34] Y. Shtessel, C. Edwards, L. Fridman, and A. Levant, *Introduction: Intuitive Theory of Sliding Mode Control*. New York, NY: Springer New York, 2014, pp. 1–42. [Online]. Available: https://doi.org/10.1007/978-0-8176-4893-0_1